

Detailed Abundances of Planet-Hosting Open Clusters. The Praesepe (Beehive) Cluster*

George Vejar¹, Simon C. Schuler², and Keivan G. Stassun¹

ABSTRACT

It is not yet fully understood how planet formation affects the properties of host stars, in or out of a cluster; however, abundance trends can help us understand these processes. We present a detailed chemical abundance analysis of six stars in Praesepe, a planet-hosting open cluster. Pr0201 is known to host a close-in (period of 4.4 days) giant planet (mass of $0.54M_J$), while the other five cluster members in our sample (Pr0133, Pr0081, Pr0208, Pr0051, and Pr0076) have no detected planets according to RV measurements. Using high-resolution, high signal-to-noise echelle spectra obtained with Keck/HIRES and a novel approach to equivalent width measurements (XSpect-EW), we derived abundances of up to 20 elements spanning a range of condensation temperatures (T_C). We find a mean cluster metallicity of $[Fe/H] = +0.21 \pm 0.02$ dex, in agreement with most previous determinations. We find most of our elements show a $[X/Fe]$ scatter of ~ 0.02 - 0.03 dex and conclude that our stellar sample is chemically homogeneous. The T_C slope for the cluster mean abundances is consistent with zero and none of the stars in our sample exhibit individually a statistically significant T_C slope. Using a planet engulfment model, we find that the planet-host, Pr0201, shows no evidence of significant enrichment in its refractory elements when compared to the cluster mean that would be consistent with a planetary accretion scenario.

Subject headings: planetary systems: formation — stars: abundances — stars: atmospheres — stars: individual (Pr0201, Pr0133, Pr0208, Pr0081, Pr0051, Pr0076)

1. Introduction

It has been over a decade now since the discoveries of Meléndez et al. (2009) and Ramírez et al. (2009) suggesting that the formation of our solar system’s planets have imprinted a measurable trend on the elemental abundances of the Sun. This trend, known as the condensation temperature (T_C) trend, can be influenced in various ways depending on the formation and evolution of the planetary system. Planet formation may reduce abundances in refractory elements ($T_C > 900K$), imparting a negative trend on abundances vs T_C since refractory-depleted material can still be accreted by the host star during the lifetime of the protoplanetary disk (Saffe et al. 2017). Planets in orbit can also be engulfed by their host star, which in turn could result in a positive slope since the star is accreting refractory-rich material into its outer layers

¹Vanderbilt University, Department of Physics & Astronomy, 6301 Stevenson Center Ln., Nashville, TN 37235, USA

²University of Tampa, Department of Chemistry, Biochemistry, and Physics, 401 W. Kennedy Blvd, Tampa, FL 33606, USA

*The data presented herein were obtained at the W. M. Keck Observatory, which is operated as a scientific partnership among the California Institute of Technology, the University of California and the National Aeronautics and Space Administration. The Observatory was made possible by the generous financial support of the W. M. Keck Foundation.

(Mack et al. 2014). The T_C slope can inform us on the amount of planetary material sequestered or accreted and help us determine if planet formation has occurred in the first place, in cases where planets have not been detected by other means. Planetary signatures and T_C trends have been studied by numerous groups making use of wide binary systems with at least one known planet in order to take advantage of the assumption that they formed from the same molecular cloud and any differences in their abundances would be due to planet formation (Ramírez et al. 2011; Mack et al. 2014; Tucci Maia et al. 2014; Biazzo et al. 2015; Ramírez et al. 2015; Saffe et al. 2015; Teske et al. 2015; Mack et al. 2016; Saffe et al. 2017; Ramírez et al. 2019). In this work, we apply similar methods to another chemically homogeneous stellar population: the Praesepe Open Cluster.

Open clusters are important laboratories for understanding a broad range of astrophysical phenomena. They have been used to study Galactic chemical evolution (Boesgaard et al. 2020; Anthony-Twarog et al. 2018), the structure and evolution of the Galactic disk (Reddy et al. 2015; MacLean et al. 2015), stellar physics (Davis et al. 2019; Schuler et al. 2009), and light element abundances (Boesgaard et al. 2016; François et al. 2013), to name a few. The basis of all these studies is the assumption that open clusters are stellar conglomerates containing coeval stars that form out of a well-mixed molecular cloud. This implies that the stars in a given open cluster are the same age and have the same primordial compositions. These properties allow for the systematic determination of their ages (Maurya & Joshi 2020; Sandquist et al. 2016), distances (Monteiro & Dias 2019; González-Díaz et al. 2019), kinematic properties (Maurya & Joshi 2020; Geller et al. 2015), and detailed compositions (Lum & Boesgaard 2019; Liu et al. 2016). There may be more useful information available about the cluster environment than there would be about a wide binary system, such as more accurate age determinations. A cluster can provide these advantages and many more stars to analyze in the context of exoplanets.

According to Meibom et al. (2013), planets in stellar clusters may be just as likely as planets around field stars, but a cluster environment can also be hostile to the formation of planets and currently there are only tens of known planets in open clusters (Cai et al. 2019). The main difference between field and cluster stars comes in the effect of the chaotic cluster environment on the formation process (protoplanetary disk) or already formed systems. O/B stars emit high energy FUV photons that can photoevaporate nearby circumstellar disks, limiting planet formation timescales (Anderson et al. 2013; Haworth et al. 2018; Winter et al. 2018). Stellar fly-by’s are frequent in the first 1-2 Myr after cluster formation which can lead to smaller systems (< 5.5 AU in size) affecting 12-20% of stars in the lifetime of a cluster similar to Praesepe (Pfalzner et al. 2018). Flybys can also eject planets from a system with an efficiency of a few percent to $\sim 10\%$ depending on semi-major axis of the planet, mass of the host star, and age of the cluster (Fujii & Hori 2019). Gas expulsion from stellar winds of massive stars or supernova explosions can cause a cluster to become supervirial and boost ejection rates as the cluster reestablishes virial equilibrium (Zheng et al. 2015). In low density environments (2k stars in 1pc virial radius), survival rates for systems containing multiple Jupiter-sized planets could be about 84% and 90% for Earth-only systems in the first 50 Myr (Cai et al. 2017). Based off estimates of the specific-free floating planet production rate from Pacucci et al. (2013), Praesepe could have produced more than 1500 free floating planets. Aside from cluster environment, intra-system dynamics/evolution will also affect a fraction of surviving planetary systems such as: planetary migration (Mayor & Queloz 1995; Lin et al. 1996), Kozai-Lidov effect (Naoz 2016), and planet-planet scattering (Johansen et al. 2012) depending on the structure of the system. The effectiveness of these mechanisms depends heavily on the size and structure of the cluster.

In this paper, we present the analysis of detailed abundance trends for six stars in Praesepe, a planet-hosting open cluster. In Section 2, we describe our sample, observations/data, spectral analysis including

our novel approach to measuring absorption line EWs, and verify our methods. In Section 3, we compare our results to the literature and present the derived stellar abundances and observed trends. In Section 4, we discuss our results in the context of a simple model for how the accretion of Earth-like rocky planets would affect refractory elemental abundances as a function of T_C and atomic number. Finally, we briefly summarize the main conclusions in Section 5.

2. Data and Analysis

2.1. Stellar Sample

Stars in Praesepe are of special interest due to the discovery of planets around a number of its members (Quinn et al. 2012; Cai et al. 2019). Praesepe is home to ~ 1000 stars, is relatively close by at 182 pc (Cantat-Gaudin et al. 2018), and has an age of ~ 600 Myr (Delorme et al. 2011), making it a strong candidate for high resolution spectroscopy of main sequence sun-like stars. It has the highest metallicity ($[\text{Fe}/\text{H}] = +0.21 \pm 0.01$ dex) of any nearby open cluster according to D’Orazi et al. (2020), which can increase the likelihood of giant planet formation (Johnson et al. 2010) if the metallicity correlation applies to stars in open clusters.

The six stars in our sample consist of a planet-host, Pr0201, and five non-hosts: Pr0133, Pr0081, Pr0076, Pr0051, and Pr0208. The data used in this study are a combination of spectra acquired by our group in 2013 and high-quality Keck Observatory Archive (KOA) spectra taken at an earlier time, all of which are publicly available. While other planet-hosts exist within Praesepe, we only acquired data for Pr0201. The derived temperatures (see Sections 2.3 and 2.4) for our stars cover ~ 500 K with spectral classes between G5 and F8 shown in Table 1. Half of our stars have temperatures within 100 K from the Sun and the other half are hotter with temperatures ~ 6100 K. Five out of the six stars have similar surface gravity estimates ranging from 4.34 to 4.44 dex and errors of about 0.10 dex. Pr0133 is an exception having a much lower surface gravity of 4.18 dex. The metallicity of our stars ranges between 0.16 and 0.26 with an average of $+0.21 \pm 0.02$ dex. In Figure 1, we show broadband SED fits (using the methodology of Stassun & Torres 2016) for two of our stars which are also consistent with our spectral analysis.

Table 1. Stellar Parameters^a

	Pr0201	Pr0133	Pr0208	Pr0081	Pr0051	Pr0076 (2003)	Pr0076 (2013)
$T_{\text{eff}}(\text{K})$	6168 ± 35	6067 ± 60	5869 ± 46	5731 ± 42	6017 ± 27	5789 ± 72	5748 ± 24
$\log g$ (cgs)	4.34 ± 0.10	4.18 ± 0.12	4.37 ± 0.13	4.44 ± 0.11	4.40 ± 0.07	4.48 ± 0.12	4.44 ± 0.07
$[\text{Fe}/\text{H}]$	0.23 ± 0.05	0.19 ± 0.06	0.26 ± 0.07	0.18 ± 0.06	0.16 ± 0.03	0.25 ± 0.06	0.22 ± 0.05
ξ (km s^{-1})	1.52 ± 0.06	1.74 ± 0.11	1.53 ± 0.07	1.41 ± 0.06	1.54 ± 0.05	1.33 ± 0.04	1.35 ± 0.03

^a Adopted solar parameters: $T_{\text{eff}} = 5777$ K, $\log g = 4.44$, and $\xi = 1.38$ km s^{-1} .

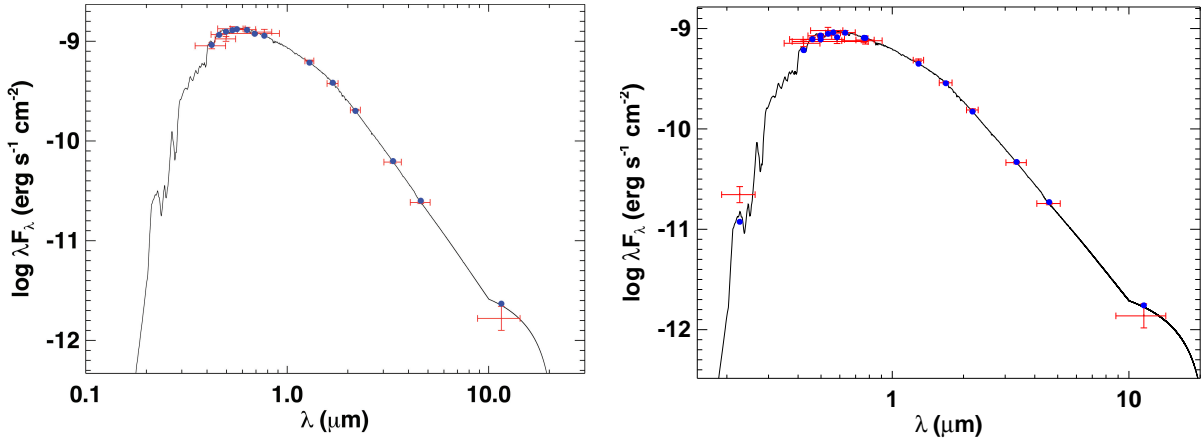


Fig. 1.— Spectral Energy Distributions for two representative targets in our study sample. Red symbols represent the broadband fluxes drawn from GALEX (Martin et al. 2003), APASS (Henden et al. 2009), 2MASS (Skrutskie et al. 2006), and WISE (Wright et al. 2010). Black curve is the best fitting Kurucz atmosphere model. Blue symbols are the model fluxes corresponding to each of the observed passbands. The integrated bolometric fluxes together with the *Gaia* DR2 parallax (Gaia Collaboration et al. 2018) yields the stellar radii. (Left) Pr0201: Reduced $\chi^2 = 2.1$, best fit extinction is $A_V = 0.072 \pm 0.024$, resulting in a bolometric flux at Earth of $F_{bol} = 1.77 \pm 0.03 \times 10^{-9} \text{ erg s}^{-1} \text{ cm}^{-2}$, giving a radius of $R = 1.166 \pm 0.022 R_\odot$. (Right) Pr0051: Reduced $\chi^2 = 1.2$, best fit extinction is $A_V = 0.07 \pm 0.03$, resulting in a bolometric flux at Earth of $F_{bol} = 1.241 \pm 0.029 \times 10^{-9} \text{ erg s}^{-1} \text{ cm}^{-2}$, giving a radius of $R = 1.086 \pm 0.019 R_\odot$.

2.2. Data Acquisition

Three of the six stars (Pr0201, Pr0051, and Pr0076) were observed on UT 2013 December 9 with the HIRES echelle spectrograph (Vogt et al. 1994) in the $R = \lambda/\Delta\lambda = 72,000$ mode on the 10-m Keck I telescope. We used the kv418 filter combined with the B2 slit setting ($0''.574 \times 7''$) and 2×1 binning; the spectra cover a wavelength range of 4600–9000Å. One exposure was taken for each star, with an integration time of 1200 s for Pr0201 and 2100 s for Pr0051 and Pr0076 individually. The signal-to-noise ratio (S/N) in the continuum near 6700Å for Pr0201 and Pr0051 is ~ 300 , and for Pr0076, it is ~ 250 .

For the remaining three stars, Pr0133, Pr0208, and Pr0081, we obtained raw data files from the KOA. These spectra, which we will collectively refer to as archive spectra, were taken in UT 2003 in January and February belonging to program ID H39aH and H47aH; the data are fully described in Boesgaard et al. (2013). We also obtained an archive spectrum for Pr0076 from the same program to verify that our analysis produces consistent results between these different sets of spectra. In our final results we report the stellar parameters and abundances for Pr0076 from both data sets and adopt the results from data taken in 2013. The archive spectra covered a smaller wavelength range (5650–8090Å) than our new spectra and were obtained in the $R = 48,000$ mode. One exposure was taken for each star with an integration time of 840 s for Pr0133, 1200 s for Pr0208, 1500 s for Pr0076, and 1500 s for Pr0081. The S/N in the continuum near 6700Å for these spectra is ~ 220 .

All of the data were reduced consistently using the MAKEE data reduction software. We required a solar spectrum to derive the solar abundances used to determine the abundances of our target stars relative to the

Sun. For this purpose, we used the high-quality Keck/HIRES solar spectrum ($S/N \sim 800$ near 6700\AA) from Schuler et al. (2015) obtained in 2010 June in the $R=50,000$ mode over the wavelength range $3750\text{--}8170\text{\AA}$. A sample region of the spectra used is shown in Figure 2 for Pr0076 from both data sets in comparison to the solar spectrum.

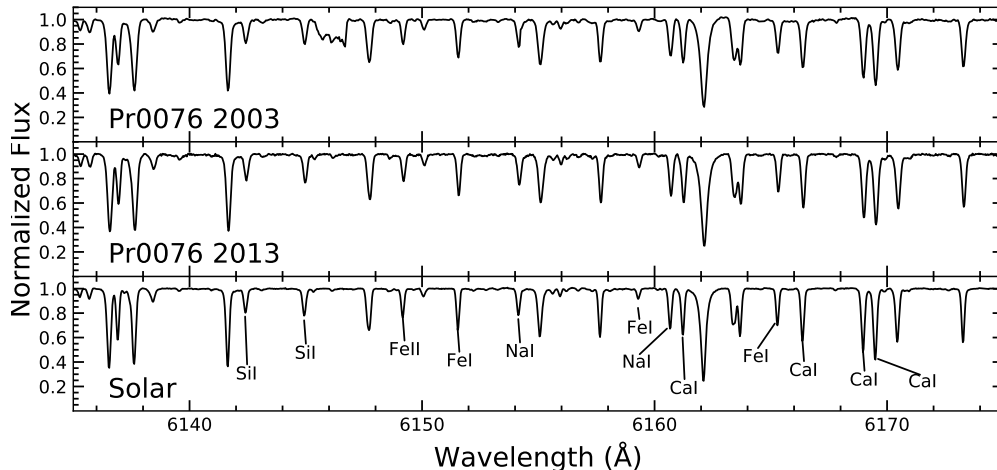


Fig. 2.— Sample Keck/HIRES spectra for Pr0076 and the sun, spanning a wavelength range of $\sim 6135 - 6175 \text{\AA}$. Top panel represents the archive data, middle panel represents data taken in 2013, and bottom panel shows the solar spectrum used. Marked absorption lines are those measured within this range.

2.3. Abundance and Stellar Parameter Determination

We have derived chemical abundances relative to solar ($[X/H]$) for up to 20 elements in each of our stars. For our analysis, the adopted solar parameters were $T_{\text{eff}} = 5777 \text{ K}$, $\log g = 4.44$, and $\xi = 1.38 \text{ km s}^{-1}$. A sample of the adopted line lists, equivalent widths (EWs), and $\log(N)$ line-by-line abundances for each element are given in Table 2. We derived abundances from measurements of EWs of atomic absorption lines in combination with MOOG, an LTE spectral analysis package (Snedden 1973, version 2014) and ATLAS9 stellar atmosphere models (Kurucz 1993). For the archive spectra, we used an abbreviated line list excluding lines not found in those spectra. To determine the stellar parameters of each star, we require the excitation and ionization balance of Fe I and Fe II lines. Atomic excitation energies (χ) and transition probabilities ($\log gf$) were taken from Mack et al. (2014). For the odd- Z elements Sc, V, Mn, and Co, hyper-fine structure (hfs) effects (Prochaska & McWilliam 2000) are taken into account for strong lines through spectral synthesis incorporating hfs components; the resulting abundances are listed in Table 3. The hfs components were obtained from Johnson et al. (2006), and line lists for regions encompassing each feature were taken from VALD (Piskunov et al. 1995; Kupka et al. 1999). Adopted Sc, V, Mn, and Co abundances were derived from the hfs analysis and lines with EWs where hfs effects are negligible. The general abundance and error analysis method is detailed in Schuler et al. (2011b), with new methods used for our current analysis detailed below.

Table 2. Lines Measured, Equivalent Widths, and Abundances

Ion	λ (Å)	χ (eV)	log gf	Solar		Pr0201		Pr0133		Pr0208		Pr0081		Pr0051		Pr0076	
				EW $_{\odot}$	log N_{\odot}	EW	log N	EW	log N	EW	log N	EW	log N	EW	log N	EW	log N
C I	5052.167	7.685	-1.304	31.58	8.417	48.52	8.481	-	-	-	-	-	-	44.66	8.507	-	-
	5380.337	7.685	-1.615	19.37	8.444	33.17	8.531	-	-	-	-	-	-	30.44	8.566	20.54	8.481
	6587.61	8.537	-1.021	12.2	8.358	28.46	8.565	20.64	8.387	20.58	8.567	14.05	8.454	19.24	8.43	12.22	8.358
	7111.469	8.64	-1.074	10.53	8.431	23.78	8.596	12.28	8.24	15.3	8.544	13.8	8.598	-	-	10.75	8.443
N I	7113.179	8.647	-0.762	22.81	8.563	40.39	8.642	30.7	8.482	26.88	8.581	26.74	8.694	30.7	8.561	24.98	8.632
	7468.313	10.336	-0.189	4.18	8.131	9.48	8.195	-	-	-	-	-	-	7.64	8.21	-	-
O I	6300.304	0.0	-9.72	5.10	8.838	4.96	8.930	-	-	-	-	-	-	-	-	8.44	9.141
	7775.39	9.15	0.001	45.45	8.806	84.57	9.078	84.38	9.139	61.74	9.007	58.58	9.097	67.51	8.951	51.79	8.96
Na I	7774.17	9.15	0.223	64.78	8.925	105.5	9.139	95.89	9.072	77.69	9.037	64.0	8.968	86.72	9.013	64.3	8.96
	7771.94	9.15	0.369	69.65	8.856	119.2	9.16	106.3	9.076	86.34	9.018	72.46	8.956	98.46	9.024	74.15	8.97
	5682.633	2.102	-0.7	98.56	6.282	102.5	6.552	-	-	116.8	6.555	-	-	99.82	6.419	119.2	6.524
	6154.226	2.102	-1.56	36.15	6.267	35.74	6.449	35.3	6.359	47.67	6.49	45.52	6.391	37.5	6.403	49.84	6.466
Mg I	6160.747	2.104	-1.26	54.69	6.255	49.66	6.374	51.33	6.317	64.53	6.43	61.46	6.321	54.25	6.362	67.11	6.411
	4730.029	4.346	-2.523	66.13	7.802	60.68	7.927	-	-	-	-	-	-	67.72	7.942	81.46	8.009
Si I	5711.088	4.346	-1.833	103.6	7.597	96.82	7.725	-	-	117.8	7.827	-	-	103.6	7.718	119.7	7.798
	6965.409	5.753	-1.51	-	-	-	-	-	-	25.88	7.34	-	-	-	-	-	-
Al I	6841.19	5.753	-1.61	64.3	7.849	69.54	8.004	77.19	8.063	85.91	8.139	-	-	68.45	7.942	74.84	8.08
	6696.023	3.143	-1.347	37.33	6.253	-	-	-	-	47.45	6.453	44.71	6.348	39.17	6.39	51.94	6.47
Si I	6698.673	3.143	-1.647	21.1	6.222	18.94	6.339	20.1	6.292	27.89	6.413	27.36	6.34	22.68	6.366	29.37	6.39
	5701.405	4.93	-1.581	37.85	7.087	39.86	7.236	-	-	-	-	-	-	41.87	7.216	47.47	7.266
	5690.425	4.93	-1.769	50.48	7.485	54.33	7.66	-	-	59.0	7.641	-	-	51.69	7.563	57.96	7.621
	5708.4	4.954	-1.034	75.82	7.14	84.46	7.388	-	-	90.55	7.375	-	-	80.76	7.268	91.02	7.378
S I	5772.149	5.082	-1.358	50.81	7.213	58.97	7.445	59.77	7.384	66.03	7.466	62.82	7.402	56.25	7.35	63.21	7.42
	7405.772	5.614	-0.313	89.3	7.108	100.7	7.352	102.1	7.332	104.6	7.326	106.4	7.324	100.7	7.289	106.3	7.34
	6125.021	5.614	-1.464	32.55	7.48	39.8	7.688	39.12	7.62	41.65	7.658	39.71	7.614	38.83	7.631	41.96	7.657
	6244.466	5.616	-1.093	44.9	7.316	54.31	7.54	53.57	7.477	58.57	7.539	55.23	7.479	53.51	7.484	56.47	7.505
S I	6243.815	5.616	-1.242	44.62	7.46	53.32	7.675	55.52	7.655	57.63	7.675	53.49	7.604	48.09	7.555	62.3	7.734
	6145.016	5.616	-1.31	39.69	7.45	46.7	7.644	42.13	7.518	53.6	7.685	43.08	7.516	44.76	7.572	48.16	7.6
	6142.483	5.619	-1.295	33.85	7.339	39.73	7.522	35.73	7.397	41.73	7.495	39.28	7.443	38.38	7.459	43.42	7.516
	6848.58	5.863	-1.524	17.25	7.401	21.13	7.572	19.82	7.485	23.61	7.584	23.82	7.582	19.27	7.491	24.55	7.602
S I	6414.98	5.871	-1.035	46.89	7.484	55.2	7.671	-	-	-	-	-	-	54.52	7.622	59.12	7.665
	7003.569	5.964	-0.937	57.28	7.606	61.99	7.74	68.65	7.794	77.06	7.873	66.17	7.734	59.56	7.669	62.59	7.697
K I	6741.628	5.984	-1.428	15.06	7.344	20.56	7.56	19.67	7.49	22.05	7.553	19.79	7.491	18.54	7.477	20.47	7.511
	4694.113	6.525	-1.77	11.0	7.311	13.81	7.27	-	-	-	-	-	-	16.24	7.419	13.26	7.423
Ca I	4695.443	6.525	-1.92	6.13	7.167	11.15	7.307	-	-	-	-	-	-	9.21	7.267	9.29	7.382
	6757.171	7.87	-0.31	14.14	7.197	34.72	7.514	28.69	7.393	23.76	7.438	-	-	25.91	7.402	19.24	7.394
Ca I	7698.98	0.0	-0.17	155.6	5.278	156.3	5.617	164.0	5.611	45.12	6.535	171.8	5.397	164.8	5.55	174.6	5.457
	6572.779	2.0	-4.24	33.23	6.252	22.26	6.404	26.57	6.319	45.12	6.535	47.48	6.438	28.67	6.397	47.77	6.467
	6166.439	2.521	-1.142	70.02	6.281	68.18	6.487	69.96	6.409	83.04	6.522	82.72	6.441	73.04	6.458	84.55	6.496
	6169.042	2.523	-0.797	91.23	6.267	90.34	6.503	94.6	6.472	105.5	6.519	108.7	6.481	95.54	6.465	111.9	6.556
	6161.297	2.523	-1.266	62.73	6.291	55.6	6.408	57.2	6.327	72.38	6.481	70.25	6.372	62.23	6.414	77.07	6.505

Table 2—Continued

Ion	λ (Å)	χ (eV)	Solar		Pr0201		Pr0133		Pr0208		Pr0081		Pr0051		Pr0076	
			EW \odot	log N_{\odot}	EW	log N	EW	log N	EW	log N	EW	log N	EW	log N	EW	log N
Sc II	6169.563	2.526	-0.478	6.203	105.7	6.423	114.8	6.471	117.9	6.375	128.9	6.419	110.6	6.367	130.2	6.467
	7326.145	2.933	-0.208	109.5	6.217	109.3	6.465	—	—	—	—	—	113.9	6.405	132.1	6.48
	5867.562	2.933	-1.57	23.79	6.288	21.84	6.448	23.51	6.396	32.43	6.517	6.446	24.85	6.439	36.48	6.533
	6604.601	1.357	-1.309	36.77	3.217	41.01	3.319	39.38	3.124	43.33	3.377	3.362	40.08	3.295	43.39	3.415
	6320.851	1.5	-1.819	9.12	3.102	11.35	3.24	—	—	11.43	3.261	—	9.38	3.144	—	—
Ti I	6245.637	1.507	-1.03	34.46	3.058	38.73	3.158	36.45	2.952	39.43	3.191	3.135	35.55	3.094	38.06	3.2
	5039.957	0.021	-1.13	72.88	4.688	63.51	4.915	—	—	—	—	—	71.56	4.888	87.26	4.939
	5210.385	0.048	-0.884	87.96	4.747	77.02	4.925	—	—	—	—	—	84.93	4.898	102.0	4.989
	5064.653	0.048	-0.991	88.13	4.882	79.82	5.108	—	—	—	—	—	86.6	5.061	—	—
	5024.844	0.818	-0.602	70.96	4.924	65.67	5.181	—	—	—	—	—	68.36	5.074	84.73	5.167
Ti II	5022.868	0.826	-0.434	69.99	4.745	61.11	4.938	—	—	—	—	—	69.0	4.926	83.53	4.983
	5739.469	2.249	-0.6	8.24	4.825	—	—	—	—	11.67	5.061	—	—	—	12.64	5.01
	5866.451	1.067	-0.84	47.33	4.901	37.04	5.078	40.2	4.959	59.03	5.159	5.118	42.58	5.033	61.57	5.115
	6261.098	1.43	-0.479	48.81	4.903	40.65	5.097	42.08	4.956	58.6	5.122	5.034	44.9	5.035	62.91	5.112
	6258.102	1.443	-0.355	51.46	4.839	42.9	5.025	43.19	4.864	60.88	5.048	5.007	47.35	4.966	64.86	5.036
V I	6091.171	2.267	-0.423	12.84	4.864	12.15	5.127	—	—	—	—	—	12.33	5.024	23.92	5.172
	6098.658	3.062	-0.01	5.72	4.835	—	—	—	—	8.8	5.093	5.079	—	—	11.15	5.132
	7138.906	1.443	-1.59	6.34	4.825	—	—	—	—	—	—	—	—	—	11.07	5.06
	5154.068	1.566	-1.75	73.94	5.045	86.31	5.273	—	—	—	—	—	83.21	5.197	80.56	5.253
	5381.021	1.566	-1.92	60.55	4.933	72.6	5.15	—	—	—	—	—	68.14	5.059	69.83	5.186
Cr I	5336.786	1.582	-1.59	71.81	4.841	83.84	5.057	—	—	—	—	—	79.92	4.969	78.87	5.055
	4779.985	2.048	-1.26	63.97	4.859	75.92	5.066	—	—	—	—	—	72.79	4.999	67.48	5.002
	6285.15	0.275	-1.51	10.22	3.844	6.71	4.065	—	—	14.86	4.125	3.992	7.83	3.978	17.47	4.077
	6251.827	0.287	-1.34	13.46	3.824	8.9	4.041	—	—	17.94	4.065	4.029	11.25	3.995	24.85	4.114
	6224.529	0.287	-2.01	4.9	4.018	—	—	—	—	—	—	—	—	—	9.64	4.298
Mn I	6243.105	0.301	-0.98	28.1	3.879	18.71	4.067	22.53	3.97	35.54	4.112	4.102	23.92	4.041	43.85	4.141
	6111.645	1.043	-0.715	10.09	3.822	10.95	4.232	11.57	4.086	16.87	4.164	4.041	10.48	4.072	20.07	4.143
	5737.059	1.064	-0.74	11.14	3.938	7.52	4.119	—	—	13.46	4.118	—	10.11	4.121	15.13	4.064
	5727.048	1.081	-0.012	38.13	3.93	27.15	4.071	—	—	47.27	4.16	—	34.47	4.079	56.29	4.224
	6081.441	1.051	-0.579	14.95	3.892	—	—	—	—	—	—	—	12.94	4.048	27.06	4.187
Mn I	6090.214	1.081	-0.062	32.8	3.851	27.53	4.106	—	—	—	—	—	29.91	4.015	47.35	4.088
	6330.091	0.941	-2.92	27.03	5.631	19.96	5.835	22.6	5.722	34.39	5.859	5.81	24.57	5.804	40.18	5.858
	7400.249	2.9	-0.111	75.93	5.569	73.08	5.775	76.58	5.708	94.81	5.896	5.838	80.61	5.778	93.11	5.826
	5787.918	3.322	-0.083	45.16	5.51	45.24	5.744	—	—	—	—	—	50.71	5.739	62.14	5.789
	5783.85	3.322	-0.295	44.18	5.705	40.72	5.875	45.2	5.846	58.87	5.997	5.904	47.73	5.901	59.62	5.959
Mn I	5783.063	3.323	-0.5	30.73	5.656	29.43	5.859	29.03	5.742	—	—	—	32.97	5.838	42.79	5.871
	5702.306	3.449	-0.667	23.0	5.77	21.88	5.966	—	—	—	—	—	26.3	5.983	36.76	6.049
	6978.397	3.464	0.142	58.64	5.594	59.81	5.839	58.49	5.712	77.04	5.923	5.834	61.86	5.771	76.98	5.878
	6979.795	3.464	-0.41	35.36	5.74	33.2	5.921	32.11	5.794	43.8	5.935	5.919	37.75	5.916	50.97	6.002
	5432.546	0.0	-3.795	50.91	5.465	30.39	5.538	—	—	—	—	—	39.95	5.54	69.84	5.771
5399.499	3.853	-0.287	37.61	5.518	37.5	5.739	—	—	—	—	—	39.15	5.677	52.82	5.785	

Table 2—Continued

Ion	λ (Å)	χ (eV)	log gf	Solar		Pr0201		Pr0133		Pr0208		Pr0081		Pr0051		Pr0076	
				EW $_{\odot}$	log N_{\odot}	EW	log N	EW	log N	EW	log N	EW	log N	EW	log N	EW	log N
Fe I	4779.439	3.42	-2.02	39.79	7.237	38.25	7.464	—	—	—	—	—	—	41.27	7.265	49.46	7.415
	4788.757	3.24	-1.76	65.33	7.29	65.69	7.558	—	—	—	—	—	—	67.74	7.337	75.06	7.480
	5054.643	3.64	-1.92	39.03	7.315	38.24	7.544	—	—	—	—	—	—	38.66	7.308	49.90	7.513
	5322.041	2.28	-2.8	61.14	7.267	56.99	7.503	—	—	—	—	—	—	60.04	7.246	—	—
	5379.574	3.69	-1.51	61.2	7.344	63.69	7.629	—	—	—	—	—	—	62.16	7.361	71.26	7.526
	5522.447	4.21	-1.55	43.66	7.55	44.22	7.775	—	—	—	—	—	—	45.5	7.583	55.06	7.752
	5543.936	4.22	-1.14	61.98	7.469	62.55	7.697	—	—	—	—	—	—	65.73	7.534	74.13	7.683
	5546.5	4.37	-1.31	49.71	7.563	54.14	7.849	—	—	—	—	—	—	53.6	7.631	65.04	7.830
	5546.991	4.22	-1.91	25.65	7.55	25.80	7.767	—	—	—	—	—	—	27.29	7.587	37.93	7.801
	5560.207	4.43	-1.19	51.79	7.539	51.81	7.744	—	—	—	—	—	—	54.52	7.586	63.11	7.735
	5577.03	5.03	-1.55	10.15	7.459	12.23	7.718	—	—	—	—	—	—	12.11	7.545	17.71	7.734
	5579.335	4.23	-2.4	8.92	7.492	9.60	7.741	—	—	—	—	—	—	10.54	7.573	13.65	7.695
	5587.574	4.14	-1.85	32.77	7.566	34.89	7.827	—	—	—	—	—	—	35.34	7.618	42.96	7.758
	5646.684	4.26	-2.5	7.54	7.54	7.28	7.735	—	—	—	—	—	—	7.68	7.548	12.24	7.768
	5651.469	4.47	-2.0	18.0	7.674	18.73	7.896	—	—	—	—	—	—	19.4	7.715	26.76	7.895
	5652.318	4.26	-1.95	26.79	7.652	27.59	7.882	—	—	—	—	—	—	28.11	7.682	36.45	7.848
	5661.346	4.28	-1.74	22.53	7.357	23.17	7.584	—	—	—	—	—	—	24.83	7.414	32.05	7.567
	5667.518	4.18	-1.58	50.25	7.66	53.20	7.929	—	—	—	—	—	—	53.97	7.726	64.38	7.908
	5677.684	4.1	-2.7	6.7	7.53	7.39	7.797	—	—	10.95	7.817	—	—	—	—	—	—
	5679.023	4.65	-0.92	58.87	7.584	60.58	7.813	—	—	71.40	7.827	—	—	61.95	7.635	72.62	7.816
	5680.24	4.19	-2.58	9.92	7.683	9.75	7.891	—	—	14.18	7.911	—	—	9.05	7.638	15.66	7.906
	5731.762	4.26	-1.3	57.03	7.576	56.69	7.783	—	—	66.22	7.768	—	—	61.82	7.659	71.12	7.821
	5732.275	4.99	-1.56	13.43	7.567	15.11	7.799	—	—	17.84	7.753	—	—	16.41	7.67	19.35	7.753
	5741.846	4.26	-1.85	31.14	7.643	34.40	7.921	—	—	40.82	7.874	—	—	34.98	7.721	43.17	7.871
	5752.032	4.55	-1.18	54.08	7.667	54.90	7.882	—	—	68.86	7.950	—	—	56.98	7.717	65.96	7.870
	5775.081	4.22	-1.3	58.13	7.556	59.23	7.790	61.45	7.730	72.73	7.840	—	—	61.02	7.606	71.72	7.793
	5778.45	2.59	-3.48	21.27	7.42	18.63	7.658	21.06	7.633	26.92	7.626	—	—	21.1	7.415	32.68	7.668
	5809.218	3.88	-1.84	49.01	7.61	47.99	7.822	52.62	7.807	62.60	7.885	—	—	50.32	7.634	61.91	7.836
	5934.655	3.93	-1.17	74.38	7.431	75.30	7.679	76.95	7.584	89.73	7.722	—	—	76.91	7.475	89.22	7.687
	6078.999	4.65	-1.12	45.07	7.535	50.94	7.831	—	—	—	—	—	—	49.91	7.62	56.95	7.740
	6085.259	2.76	-3.1	42.75	7.646	38.93	7.869	—	—	—	—	—	—	40.59	7.605	55.38	7.860
	6098.245	4.56	-1.88	15.83	7.553	18.10	7.819	19.53	7.803	25.52	7.863	—	—	18.08	7.623	25.01	7.800
	6151.617	2.18	-3.3	49.27	7.384	43.93	7.616	47.49	7.559	57.73	7.584	—	—	48.06	7.362	61.57	7.585
	6159.368	4.61	-1.97	12.49	7.568	14.80	7.846	16.39	7.842	23.85	7.957	—	—	14.42	7.641	19.69	7.800
	6165.36	4.14	-1.47	43.68	7.373	42.54	7.569	46.05	7.547	54.50	7.601	—	—	47.24	7.437	55.32	7.576
	6173.336	2.22	-2.88	67.93	7.337	65.82	7.612	72.32	7.575	80.69	7.596	—	—	68.7	7.351	—	—
	6187.987	3.94	-1.72	46.71	7.487	44.33	7.671	—	—	—	—	—	—	48.54	7.52	61.21	7.739
	6220.776	3.88	-2.46	19.45	7.588	14.92	7.681	14.36	7.593	23.50	7.747	—	—	19.8	7.598	26.27	7.753
	6226.73	3.88	-2.22	28.6	7.573	26.42	7.757	32.41	7.807	35.94	7.770	—	—	29.98	7.603	40.97	7.813
	6229.228	2.85	-2.81	37.66	7.34	36.74	7.613	38.93	7.554	49.51	7.607	—	—	39.5	7.375	51.30	7.577
	6240.645	2.22	-3.23	49.7	7.353	43.88	7.574	47.22	7.515	61.27	7.603	—	—	46.97	7.304	61.60	7.546

Table 2—Continued

Ion	λ (\AA)	χ (eV)	Solar		Pr0201		Pr0133		Pr0208		Pr0081		Pr0051		Pr0076	
			EW	$\log N_{\odot}$	EW	$\log N$	EW	$\log N$	EW	$\log N$	EW	$\log N$	EW	$\log N$	EW	$\log N$
	6293.924	4.84	13.4	7.567	16.08	7.841	—	—	—	—	—	—	17.19	7.697	21.86	7.823
	6297.793	2.22	72.68	7.277	69.31	7.528	—	—	—	—	—	—	74.83	7.317	—	—
	6322.685	2.59	75.11	7.374	73.58	7.637	75.98	7.535	93.21	7.725	88.04	7.561	78.5	7.436	93.00	7.685
	6380.743	4.19	52.09	7.473	52.38	7.692	54.71	7.640	62.72	7.688	61.46	7.609	54.09	7.508	63.76	7.673
	6392.538	2.28	16.51	7.491	11.36	7.634	15.95	7.710	21.32	7.703	22.94	7.636	13.95	7.404	23.94	7.679
	6597.557	4.79	43.46	7.567	43.98	7.761	48.28	7.763	56.30	7.820	53.77	7.726	46.52	7.726	56.49	7.790
	6608.024	2.28	16.74	7.486	16.50	7.810	16.67	7.721	21.75	7.702	24.26	7.655	15.1	7.433	26.47	7.726
	6609.11	2.56	65.5	7.411	63.50	7.671	67.39	7.602	80.11	7.696	81.71	7.648	64.31	7.389	80.18	7.657
	6627.54	4.55	27.39	7.63	29.37	7.869	32.19	7.860	37.53	7.876	35.11	7.771	28.94	7.664	38.38	7.848
	6653.85	4.15	10.09	7.552	11.73	7.845	—	—	—	—	—	—	11.33	7.609	15.14	7.748
	6703.567	2.76	37.17	7.566	31.54	7.753	35.81	7.738	47.06	7.799	48.00	7.726	36.14	7.546	50.64	7.795
	6710.316	1.49	15.91	7.513	10.90	7.706	13.84	7.719	23.01	7.798	25.97	7.740	13.74	7.439	24.77	7.734
	6713.745	4.8	20.94	7.63	23.80	7.884	22.24	7.788	29.59	7.872	30.95	7.846	23.89	7.705	31.10	7.861
	6716.222	4.58	15.11	7.564	15.93	7.785	15.08	7.699	21.11	7.787	20.08	7.699	17.36	7.637	22.43	7.772
	6725.353	4.1	17.17	7.549	16.88	7.761	17.32	7.708	24.44	7.794	26.13	7.764	18.2	7.58	25.17	7.756
	6726.666	4.61	45.83	7.493	48.91	7.739	51.63	7.706	59.60	7.759	58.57	7.688	50.25	7.569	60.41	7.740
	6733.151	4.64	26.82	7.599	28.65	7.830	29.50	7.784	35.31	7.814	35.81	7.767	29.43	7.656	38.31	7.829
	6739.52	1.56	11.32	7.321	9.01	7.589	—	—	18.43	7.656	16.99	7.487	10.47	7.283	19.18	7.572
	6745.09	4.58	7.8	7.477	9.17	7.749	—	—	14.37	7.822	—	—	8.13	7.497	13.17	7.726
	6745.957	4.08	6.66	7.531	8.09	7.847	—	—	—	—	—	—	7.96	7.616	11.74	7.796
	6750.15	2.42	73.4	7.332	69.88	7.570	72.88	7.476	85.02	7.559	87.06	7.518	73.7	7.337	88.39	7.581
	6752.716	4.64	35.72	7.505	37.19	7.724	42.02	7.743	51.91	7.830	49.08	7.727	39.67	7.58	49.57	7.753
	7114.549	2.69	7.57	7.455	6.74	7.709	—	—	11.19	7.715	14.01	7.725	9.48	7.562	11.81	7.656
	7284.835	4.14	41.49	7.561	39.72	7.744	46.28	7.777	55.41	7.838	52.31	7.726	43.28	7.593	53.79	7.771
Fe II	4620.521	2.828	53.41	7.435	67.36	7.641	—	—	—	—	—	—	64.51	7.68	57.82	7.608
	5197.577	3.23	80.04	7.387	105.30	7.775	—	—	—	—	—	—	98.31	7.746	89.86	7.672
	5234.625	3.221	2.279	7.314	105.70	7.701	—	—	—	—	—	—	98.12	7.662	89.54	7.585
	5264.812	3.23	39.51	7.308	57.43	7.571	—	—	—	—	—	—	53.91	7.617	50.27	7.616
	5414.073	3.221	25.69	7.486	40.63	7.730	—	—	—	—	—	—	36.77	7.748	31.12	7.687
	5425.257	3.199	39.8	7.536	52.66	7.695	—	—	—	—	—	—	49.66	7.746	46.86	7.762
	6084.111	3.199	20.4	7.542	31.34	7.728	—	—	—	—	—	—	27.42	7.73	25.58	7.752
	6113.322	3.221	12.35	7.628	20.74	7.831	—	—	17.90	7.841	13.98	7.756	16.98	7.8	15.65	7.820
	6149.258	3.889	36.26	7.549	51.45	7.722	52.47	7.653	48.11	7.783	38.23	7.658	46.4	7.77	39.17	7.689
	6247.557	3.892	50.89	7.459	78.65	7.848	76.92	7.696	67.16	7.755	58.06	7.673	68.38	7.815	59.82	7.727
	7222.394	3.889	18.76	7.63	24.49	7.668	31.20	7.762	—	—	22.18	7.797	27.26	7.867	21.07	7.770
	7449.335	3.889	18.06	7.686	32.46	7.930	33.91	7.896	30.34	8.011	23.90	7.924	26.7	7.931	22.45	7.889
	7711.723	3.903	44.82	7.533	66.54	7.784	72.21	7.784	59.00	7.789	53.25	7.776	59.31	7.821	50.48	7.735
Co I	5301.039	1.71	19.9	4.945	—	—	—	—	—	—	—	—	15.26	5.017	24.35	5.054
	6093.143	1.74	10.5	5.034	—	—	—	—	—	—	—	—	7.81	5.108	12.56	5.115
	6814.942	1.956	18.5	4.959	11.96	5.07	13.57	4.956	26.79	5.242	25.16	5.103	17.65	5.136	26.59	5.156
	5647.234	2.28	14.06	4.863	9.34	4.976	—	—	—	—	—	—	11.07	4.935	19.91	5.042

2.4. User Guided Equivalent Width Measurements

The EW measurement of absorption lines is performed by an in-house user guided code called eXtract from SPECTra - Equivalent Widths (XSpect-EW), specifically created for this purpose. The general process for measuring EWs of absorption lines for abundance derivations includes three main steps: normalization of the continuum, wavelength shift, and fitting the absorption lines with Gaussian or Voigt profiles to determine the EW of the lines. Each step of the process can be vulnerable to user error if done manually, as detailed in the following subsections, depending on how much care and time is given to each part of the analysis. Ideally, one would take extreme care in each of these parts within a minimal amount of time.

2.4.1. Continuum Normalization

Arguably the most important part of the EW measuring process is the ability to consistently determine the continuum of the spectrum or each spectral order. The differential Curve of Growth (CoG) abundance determination involves comparing the abundances of the star of interest to those of a standard or reference star, often the Sun; therefore, one must be able to determine the continuum in each spectral order in the same way for the star and the standard so as to minimize differences in the abundances that could arise as a result of the analysis. XSpect-EW has been designed to normalize the spectrum efficiently and accurately by using a two-step process.

Step 1: a spectrum is split into smaller pieces (referred to as selection windows), the size of which is set to larger than the typical size of the absorption lines to ensure that the selection windows do not fall entirely within a line. For example, in an optical high resolution Keck/HIRES spectrum with $R > 60k$, the width of a typical line will be 0.4–0.6 Å, so the size of the selection window could be ~ 1.6 Å. Points above 90% of the flux values within a selection window are chosen as points in the continuum (90% value can be adjusted by the user if needed).

Step 2: the chosen continuum points are used to normalize the spectrum by fitting them with a Gaussian Process (GP). A GP is a collection of random variables, any finite number of which have a joint Gaussian distribution. GPs are useful for data containing non-trivial stochastic signals or noise. A square exponential kernel (or Gaussian kernel) $k_{SE}(x, x') = A \exp[-\Gamma(x - x')^2]$ is used for the covariance function in the GP where A is the variance and Γ is the inverse lengthscale ($\Gamma = (1/2l^2)$). A variance of similar order of magnitude as the flux values is used (10^7), along with an inverse lengthscale of 0.1. After testing various values, these gave the best results for our spectra. XSpect-EW will be updated to automatically determine the variance and lengthscale values for each order in a spectrum and to have a variety of kernels available. The flux is then divided by the curve output by the GP (grey curve in Fig. 3 top panel) which normalizes the order (Fig. 3 bottom panel).

2.4.2. Wavelength Shift

Once normalization is complete, each order is wavelength shifted to the rest frame. This can be done manually by visually identifying a portion of an order in the observed spectrum, comparing it to a reference spectrum, and using software to shift the wavelength axis by the appropriate amount. Errors in this part of the process can lead to measuring the wrong lines within an order, which may show up as abundance outliers or result in higher than expected abundance errors later in the analysis.

Table 2—Continued

Ion	λ (Å)	X (eV)	log gf	Solar		Pr0201		Pr0133		Pr0208		Pr0081		Pr0051		Pr0076	
				EW	$\log N_{\odot}$	EW	$\log N$	EW	$\log N$	EW	$\log N$	EW	$\log N$	EW	$\log N$	EW	$\log N$
Ni I	6632.433	2.28	-2.0	8.7	5.012	—	—	—	—	12.44	5.262	12.04	5.146	—	—	13.42	5.217
	6643.629	1.676	-2.3	92.89	6.366	86.9	6.55	—	—	—	—	—	—	91.31	6.48	108.6	6.636
	6108.107	1.676	-2.45	65.59	6.062	57.99	6.226	58.99	6.056	72.29	6.216	76.1	6.217	60.95	6.142	74.99	6.234
	6327.593	1.676	-3.15	38.63	6.253	30.41	6.41	30.53	6.231	45.0	6.431	49.24	6.418	35.71	6.385	49.6	6.449
	5846.986	1.676	-3.21	23.29	6.017	19.29	6.236	20.53	6.09	28.38	6.21	30.43	6.157	22.39	6.188	33.95	6.251
	5748.346	1.676	-3.26	28.42	6.193	22.36	6.373	—	—	33.67	6.374	—	—	24.43	6.294	36.84	6.364
	6128.963	1.676	-3.33	25.97	6.184	20.33	6.367	20.26	6.186	31.53	6.377	34.14	6.334	21.23	6.261	36.57	6.403
	6767.768	1.826	-2.17	78.94	6.122	74.29	6.325	—	—	—	—	—	—	80.83	6.3	93.74	6.385
	6177.236	1.826	-3.5	13.77	6.154	10.98	6.358	—	—	17.26	6.347	19.21	6.31	11.82	6.269	20.82	6.373
	5754.655	1.935	-2.33	74.12	6.395	68.12	6.564	73.16	6.475	85.24	6.627	83.04	6.527	73.38	6.525	86.08	6.628
	6370.341	3.542	-1.94	13.37	6.251	12.66	6.439	—	—	20.53	6.531	16.51	6.353	12.52	6.347	17.84	6.407
	6842.035	3.658	-1.48	23.78	6.196	22.79	6.377	23.75	6.279	32.77	6.44	29.41	6.315	24.41	6.331	33.59	6.418
	6176.807	4.088	-0.26	62.48	6.161	64.01	6.372	64.73	6.277	74.79	6.398	71.56	6.305	66.65	6.324	75.28	6.395
	6111.066	4.088	-0.87	34.04	6.257	35.09	6.461	38.58	6.421	42.8	6.462	40.78	6.38	37.48	6.427	42.84	6.434
	6204.6	4.088	-1.1	21.49	6.198	22.58	6.41	23.23	6.319	28.58	6.409	28.4	6.357	23.98	6.368	30.63	6.419
	6175.36	4.089	-0.559	48.4	6.219	51.43	6.455	57.24	6.45	62.76	6.501	58.01	6.379	53.47	6.405	58.49	6.409
5760.828	4.105	-0.8	33.33	6.203	32.7	6.373	36.88	6.349	45.33	6.468	40.81	6.34	35.42	6.347	44.12	6.418	
6223.981	4.105	-0.91	29.89	6.223	29.3	6.392	29.42	6.287	37.3	6.411	35.86	6.337	30.4	6.337	38.29	6.4	
6186.709	4.105	-0.96	31.48	6.308	30.73	6.474	—	—	—	—	—	—	32.7	6.436	39.76	6.479	
6230.09	4.105	-1.26	20.34	6.342	21.26	6.55	23.48	6.499	25.19	6.507	27.29	6.507	22.03	6.494	29.4	6.568	
6378.247	4.154	-0.83	31.93	6.226	33.22	6.432	32.3	6.307	40.78	6.435	37.67	6.333	33.31	6.355	42.51	6.44	
5805.213	4.167	-0.64	40.8	6.245	40.52	6.419	41.17	6.326	47.93	6.41	49.31	6.391	42.14	6.368	51.83	6.455	
6598.593	4.236	-0.98	24.83	6.288	25.5	6.479	26.81	6.406	35.44	6.553	33.6	6.473	26.67	6.431	35.27	6.52	
6130.13	4.266	-0.96	22.71	6.262	21.08	6.394	20.97	6.289	30.91	6.489	27.64	6.373	23.01	6.37	30.98	6.459	
6635.118	4.419	-0.82	24.34	6.288	23.84	6.442	22.09	6.3	32.79	6.511	31.49	6.443	25.61	6.413	32.79	6.482	
5782.127	1.642	-1.72	77.4	4.46	63.08	4.481	67.35	4.368	83.97	4.605	88.92	4.64	68.61	4.442	88.83	4.686	
4722.153	4.03	-0.338	69.25	4.463	74.14	4.615	—	—	—	—	—	—	74.11	4.56	74.89	4.641	

Note. — This table is published in its entirety in the online journal. A portion is shown here for guidance regarding its form and content.

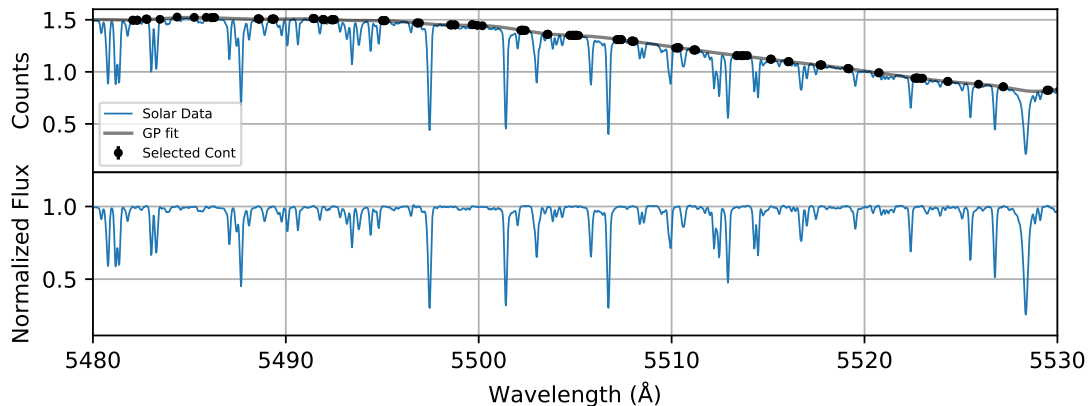


Fig. 3.— Sample section of an order within the observed solar spectrum before and after normalization. Black points are those selected as part of the continuum; black curve is the output of the Gaussian Process.

XSpec-EW makes use of a simple χ^2 minimization approach to this problem. An input spectrum is shifted to match a solar spectrum order by order. This is done by determining the median wavelength value in the order of the spectrum to be shifted, finding which order in the solar spectrum this value falls, and shifting the order to match the solar spectrum. The shift is determined by evaluating χ^2 between both orders for a range of wavelength shifts from -5 \AA to $+5 \text{ \AA}$ in steps of 0.1 \AA and selecting the shift with the minimum χ^2 value (shift ranges and resolution can be changed by user if needed). In cases where a shift cannot be determined for an order, the shifts for other orders are used to predict the shift of the missing order by linear interpolation of the shift values. A user may also manually shift any order by a specified amount for further correction if needed.

2.4.3. Equivalent Width Measurements

Measuring the EW of an absorption line generally involves fitting a Gaussian or Voigt function to the line and then integrating that function to determine the area enclosed by the curve and continuum. XSpec-EW uses a four step process for this.

Table 3. Synthesized HFS Line Abundances

Ion	λ (\AA)	χ (eV)	log gf	Solar $\log N_{\odot}$	Pr0201	Pr0133	Pr0208	Pr0081	Pr0051	Pr0076
Co I	6814.942	1.956	-1.9	–	5.07	–	–	–	–	–
	5301.039	1.71	-2.0	–	–	–	–	–	–	–
Mn I	5432.546	0.0	-3.795	5.28	5.46	–	–	–	5.41	5.55
Sc II	6604.601	1.357	-1.309	3.10	3.18	3.09	3.25	3.15	3.17	3.27
	6245.637	1.507	-1.03	3.10	3.23	3.09	3.25	3.15	3.16	3.17
V I	6111.645	1.043	-0.715	–	–	–	–	–	–	4.05
	6090.214	1.081	-0.062	3.83	4.03	–	–	–	–	4.05

Note. — isted synthesized abundances replace EW abundances from Table 2.

Step 1: the extent of the line being measured is determined. Carefully determining the extent, or width of the line at the continuum, is critical to obtaining an accurate measure of the absorption in the line. A piece of the spectrum around a selected line is trimmed from the rest of the spectrum (default set to 1.5 Å about the line center). The boundaries of the line being measured are determined by utilizing the slope of the flux values within the piece of the spectrum. These values range from a maximum or minimum near the center of the line to zero at the continuum and the core, as shown in Figure 4. Using one half of the standard deviation of the flux slope values, a range of values centered on the continuum is created. After testing various values, one half of the standard deviation gave us best results relative to hand-measured EWs. The boundaries of the absorption line are defined as the points where the slope enters this range from the maximum or minimum values to either edge of the line. At this boundary, the slope values approach zero as the flux values approach the constant continuum.

Step 2: with the boundaries defined, XSpect-EW assumes the continuum is correct and shifts the data outside the boundaries of the line (still within the 1.5 Å line window) to match the continuum, effectively isolating the line to be measured.

Step 3: the isolated absorption line and associated continuum is fed into another GP (same kernel) with a small variance of 1 and large inverse lengthscale of 100.

Step 4: the GP can produce different realizations of the data, and XSpect-EW uses this to perform a Gaussian fit to the line, repeating the process 100 times and thus producing 100 different EW measurements. The mean and standard deviation are calculated using the 100 measurements of the line. Each absorption line can be plotted and remeasured if needed, with the ability to adjust the local continuum, center of the line, and boundaries of the line.

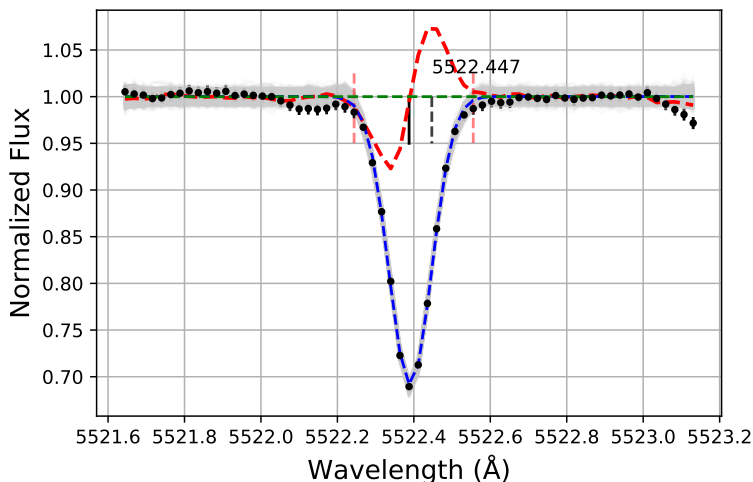


Fig. 4.— Sample plot for an Fe I line (5522.447Å) from the solar spectrum. Black dots with error bars correspond to data; grey shading shows the 1σ variance, blue curve is the Gaussian fit. Green horizontal line defines the continuum. Red curve shows the slope of the flux values (shifted to the continuum). Red vertical lines establish the boundaries of the line measured. Dashed black vertical line is the input wavelength of the line, solid vertical line is the best fit wavelength of the line.

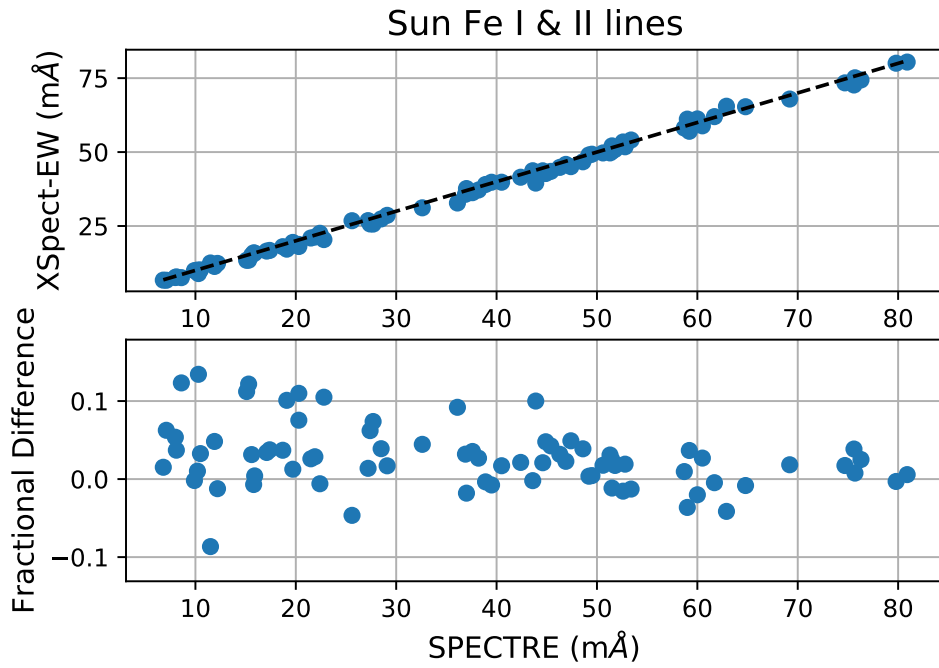


Fig. 5.— Top panel: X_Spect-EW measured lines (with some user input) plotted against hand measured EWs in SPECTRE. Dashed line is the one-to-one line. Bottom panel: Fractional difference $([X_{\text{Spect-EW}} - \text{hand}] / \text{hand})$ between X_Spect-EW and hand measured values.

2.4.4. Verification of Methodology

To verify the robustness of our new EW measuring tool, in Figure 5 we compare EWs of Fe I and Fe II lines measured in our solar spectrum with XSpec-EW and by hand with SPECTRE, a spectral analysis package (Snedden et al. 2012). All differences are $< 15\%$, with 80% of Fe lines having differences smaller than 5%. In the remaining elemental lines (not shown here), $\sim 70\%$ of lines have differences smaller than 5%. XSpec-EW requires some user input to obtain these measurements which consists of checking each automatic line fit and remeasuring problematic lines by adjusting extra parameters that characterize the absorption line. We note that this interactive functionality has been purposely built into XSpec-EW for this specific purpose. The scatter in the fractional difference of the line measurements is larger for the other elements, because those lines can generally be more difficult to measure due to the variety in the strength of the lines and proximity to other lines. A well curated line-list can be helpful for automatic line fits as strong, isolated absorption lines are easier for XSpec-EW to measure automatically. The quality of the data will also be a deciding factor in the number of lines that need to be remeasured. In this example, 17% of Fe lines and 23% of other elemental lines required remeasuring, greatly reducing the amount of time needed to measure all lines and allowing the user to focus on problematic lines to produce abundances with high precision. Lines that are remeasured are only considered based on visual inspection of the fit, not in comparison to previous measurements, since when measuring a new star no comparison would be available. The average of the Fe absolute abundances derived from the XSpec-EW and SPECTRE EWs, shown in Figure 6, agree within errors and agree with the input solar absolute abundance within MOOG of 7.50 dex. For all Fe I and II lines, we see a smaller scatter in the absolute abundances from the XSpec-EW measurements than in the SPECTRE measurements by 0.01 dex. From this we can see that XSpec-EW performs as well, if not slightly better, than a full set of hand-measured EWs from SPECTRE.

From the Fe I and Fe II abundances derived using the EWs measured with XSpec-EW, we determine an average cluster metallicity for Praesepe of 0.21 ± 0.02 dex, which is in good agreement with most past works on the cluster metallicity. In Table 4, we show the literature stellar parameter values for each star along with our own derived values. Our derived stellar parameters (T_{eff} , $\log G$, $[\text{Fe}/\text{H}]$) are also in good agreement with current literature values. The main discrepancy between our stellar parameters and literature values comes from the ξ parameter values which in general are larger than literature values, likely due to the higher ξ value adopted for the Sun in this work (1.38 km/s here, compared to lower values used in other studies)(Pace et al. 2008; Gebran et al. 2019; D’Orazi et al. 2020). A more detailed comparison of individual stars to the literature is presented in section 3.2.

3. Results

3.1. Derived Stellar Abundances

The derived elemental abundances for our targets are summarized in Table 5. Elements with only one measured absorption line have no mean and therefore no uncertainty in the mean; for those lines we have adopted the total error to be the average total error of all other elements in the star. Some elements in some stars were not measurable due to lack of spectral coverage or removal of lines that were not measurable (due to noise, blending, bad fit...etc). The errors for all stellar parameters and abundances are symmetric or close to symmetric (where $\pm\sigma_{\text{Total}}$ intervals are equal or close to equal); in all cases we conservatively adopt the larger error, except with surface gravity where we adopt the average error. The resulting differences between the archive data (2003) and our data (2013) for Pr0076 are within error bars for the derived stellar

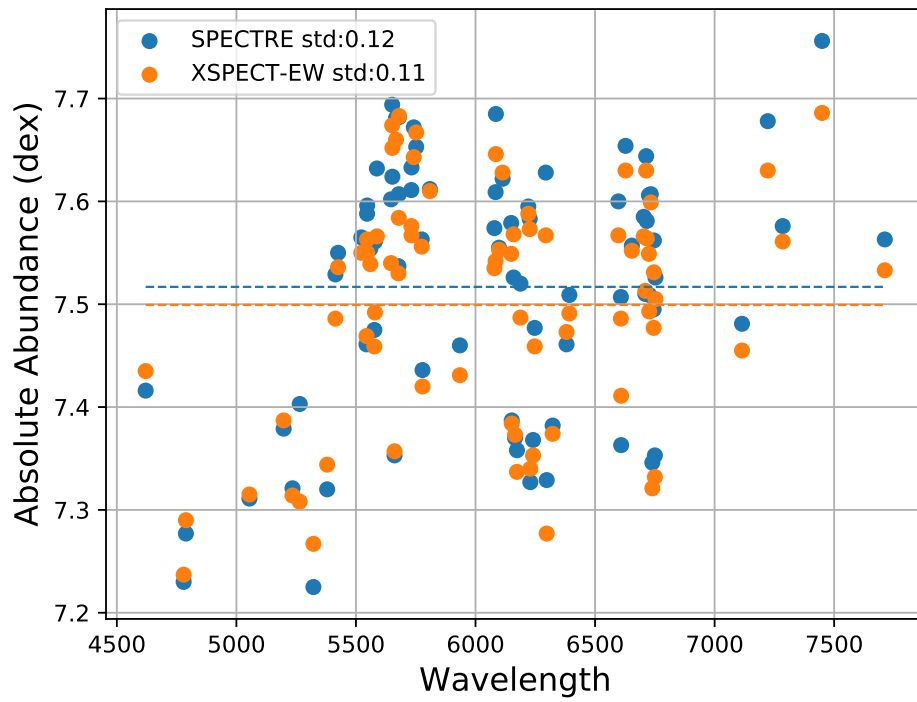


Fig. 6.— Output absolute abundances from Solar Fe I and Fe II lines shown in Figure 5 using MOOG. Blue points represent abundances from SPECTRE measurements while orange points represent abundances from XSpec-EW. The dashed lines (same colors used as for points) show the average abundances for each method.

Table 4. Comparison to Literature

Star ID alt ID	T_{eff} K	$\log G$ $\log(\text{g} \cdot \text{cm} \cdot \text{sec}^{-1})$	ξ km/s	[Fe/H] dex	Reference
Pr0201	6168 ± 35	4.34 ± 0.10	1.52 ± 0.06	0.23 ± 0.05	This work
Prae kw 418	6174 ± 50	4.41 ± 0.10	—	0.19 ± 0.04	Quinn et al. (2012)
	6062 ± 110	4.44 ± 0.07	1.27 ± 0.18	0.24 ± 0.10	Pace et al. (2008)
Pr0133	6067 ± 60	4.18 ± 0.12	1.74 ± 0.11	0.19 ± 0.06	This work
Prae kw 208	6005 ± 19	4.46 ± 0.21	1.05 ± 0.04	0.18 ± 0.03	Gebran et al. (2019)
	5997 ± 60	4.38 ± 0.20	1.40 ± 0.20	0.12 ± 0.10	Boesgaard et al. (2013)
	5993 ± 110	4.45 ± 0.07	1.52 ± 0.18	0.28 ± 0.10	Pace et al. (2008)
Pr0208	5869 ± 46	4.37 ± 0.13	1.53 ± 0.07	0.26 ± 0.07	This work
N2632-8	5977 ± 75	4.55 ± 0.15	1.30 ± 0.20	0.25 ± 0.11	D’Orazi et al. (2020)
Prae kw 432	5841 ± 73	4.40 ± 0.20	1.25 ± 0.20	0.17 ± 0.10	Boesgaard et al. (2013)
Pr0081	5731 ± 42	4.44 ± 0.11	1.41 ± 0.06	0.18 ± 0.06	This work
CPrae kw 30	5716 ± 45	4.57 ± 0.42	1.18 ± 0.04	0.12 ± 0.04	Gebran et al. (2019)
	5675 ± 111	4.44 ± 0.20	1.07 ± 0.20	0.12 ± 0.10	Boesgaard et al. (2013)
Pr0051 TYC 1395-668-1	6017 ± 27	4.40 ± 0.07	1.54 ± 0.05	0.16 ± 0.03	This work
Pr0076	5748 ± 24	4.44 ± 0.07	1.35 ± 0.03	0.22 ± 0.05	This work
Prae kw 23	5773 ± 53	4.56 ± 0.24	1.20 ± 0.04	0.20 ± 0.04	Gebran et al. (2019)
	5699 ± 79	4.43 ± 0.20	1.10 ± 0.20	0.12 ± 0.10	Boesgaard et al. (2013)

parameters and elemental abundances, as shown in Table 5. Despite the fact that we are using data of differing quality, observing conditions, instrument setup, and time of observation we are able to produce consistent results giving us great confidence in our analysis.

Fig 7 shows the abundance vs atomic number for each star and the cluster mean. Most elements have a similar spread about the mean while some (K, Sc, Co, and Cu) show a larger spread. This larger spread is likely due to the fact that these elements have a low number of lines measured, lines may be weak, noisy, or blended with other nearby lines making them difficult to measure, or some combination of these factors.

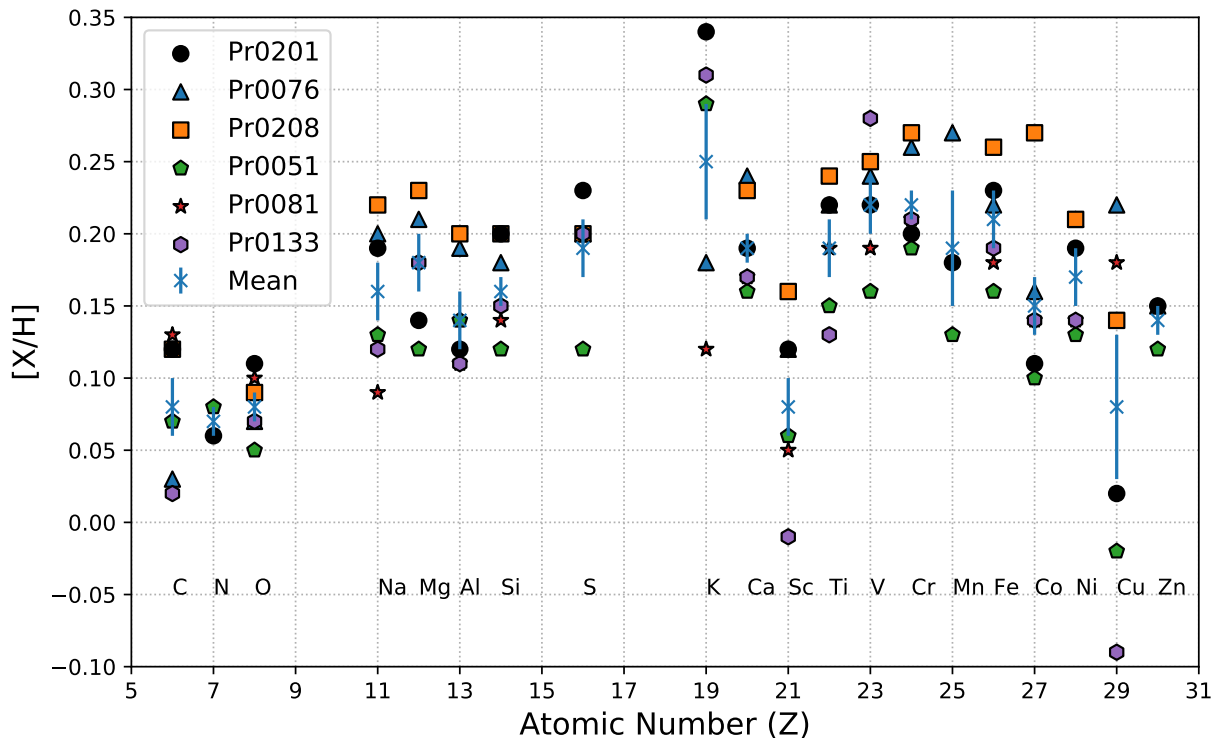


Fig. 7.— Abundances vs. atomic number (Z) for all Praesepe stars (2013 data used for Pr0076). The planet host, Pr0201, is shown as a filled circle. The typical error bar for elements is 0.05 dex (check Table 5 for specific errors). The mean for each element is shown in the blue cross along with the error in the mean.

3.1.1. Planet-Hosting Star

In order to see if the planet host, Pr0201, is different from the rest of our sample, we compare the abundances to the cluster mean. Figure 8 shows the difference between Pr0201 and the cluster mean (not including the planet host) for each derived element vs atomic number. Most elements fall between ± 0.05 dex of the cluster mean and are within errors of zero with a few exceptions. The element with the largest difference is K having an overabundance of 0.12 dex when compared to the cluster. Si, having the smallest total error of 0.01 dex, is also significantly overabundant in the planet host by 0.04 dex. The planet host shows no obvious trend in abundance vs atomic number over all measured elements.

Table 5. Stellar Abundances

	Pr0201	Pr0133	Pr0208	Pr0081	Pr0051	Pr0076 (2003)	Pr0076 (2013)
[C/H]	0.12 ± 0.03 ^b ± 0.05 ^c	0.02 ± 0.03 ± 0.06	0.12 ± 0.06 ± 0.09	0.13 ± 0.03 ± 0.05	0.07 ± 0.03 ± 0.04	0.10 ± 0.07 ± 0.09	0.03 ± 0.01 ± 0.04
[O/H]	0.11 ± 0.03 ± 0.05	0.07 ± 0.03 ± 0.07	0.09 ± 0.05 ± 0.08	0.10 ± 0.09 ± 0.11	0.05 ± 0.03 ± 0.05	...	0.07 ± 0.04 ± 0.05
[Na/H]	0.19 ± 0.02 ± 0.03	0.12 ± 0.04 ± 0.05	0.22 ± 0.04 ± 0.03	0.09 ± 0.03 ± 0.04	0.13 ± 0.01 ± 0.02	0.27 ± ... ± 0.08	0.20 ± 0.03 ± 0.03
[Mg/H]	0.14 ± 0.01 ± 0.03	0.18 ± ... ± 0.05	0.23 ± 0.03 ± 0.05	...	0.12 ± 0.01 ± 0.02	0.20 ± 0.24 ± 0.24	0.21 ± 0.01 ± 0.05
[Al/H]	0.12 ± ... ± 0.05	0.11 ± ... ± 0.05	0.20 ± 0.00 ± 0.02	0.11 ± 0.01 ± 0.01	0.14 ± 0.00 ± 0.01	...	0.19 ± 0.02 ± 0.03
[Si/H]	0.20 ± 0.01 ± 0.01	0.15 ± 0.01 ± 0.02	0.20 ± 0.01 ± 0.01	0.14 ± 0.01 ± 0.01	0.12 ± 0.01 ± 0.01	0.19 ± 0.02 ± 0.02	0.18 ± 0.01 ± 0.01
[Ca/H]	0.19 ± 0.02 ± 0.03	0.17 ± 0.01 ± 0.05	0.23 ± 0.02 ± 0.05	0.17 ± 0.02 ± 0.04	0.16 ± 0.01 ± 0.03	0.27 ± ... ± 0.08	0.24 ± 0.01 ± 0.03
[Sc/H]	0.12 ± 0.02 ± 0.05	-0.01 ± ... ± 0.05	0.16 ± 0.01 ± 0.07	0.05 ± ... ± 0.05	0.06 ± 0.01 ± 0.03	...	0.12 ± 0.05 ± 0.07
[Ti/H]	0.22 ± 0.01 ± 0.06	0.13 ± 0.01 ± 0.06	0.24 ± 0.01 ± 0.04	0.19 ± 0.03 ± 0.05	0.15 ± 0.01 ± 0.04	0.24 ± 0.03 ± 0.10	0.22 ± 0.02 ± 0.06
[V/H]	0.22 ± 0.03 ± 0.05	0.28 ± 0.05 ± 0.08	0.25 ± 0.02 ± 0.06	0.19 ± 0.02 ± 0.05	0.16 ± 0.01 ± 0.03	0.27 ± 0.03 ± 0.08	0.24 ± 0.01 ± 0.03
[Cr/H]	0.20 ± 0.01 ± 0.03	0.21 ± 0.01 ± 0.05	0.27 ± 0.03 ± 0.05	0.21 ± 0.02 ± 0.04	0.19 ± 0.01 ± 0.02	0.29 ± 0.01 ± 0.05	0.26 ± 0.01 ± 0.02
[Mn/H]	0.20 ± ... ± 0.04	0.13 ± ... ± 0.03	0.36 ± 0.01 ± 0.07	0.27 ± ... ± 0.04
[Fe/H]	0.23 ± 0.01 ± 0.05	0.19 ± 0.01 ± 0.06	0.26 ± 0.01 ± 0.07	0.18 ± 0.01 ± 0.06	0.16 ± 0.00 ± 0.03	0.25 ± 0.01 ± 0.06	0.22 ± 0.00 ± 0.05
[Co/H]	0.11 ± 0.01 ± 0.03	0.14 ± ... ± 0.05	0.27 ± 0.02 ± 0.04	0.14 ± 0.01 ± 0.03	0.10 ± 0.03 ± 0.04	0.18 ± 0.03 ± 0.07	0.16 ± 0.02 ± 0.03
[Ni/H]	0.19 ± 0.01 ± 0.02	0.14 ± 0.01 ± 0.04	0.21 ± 0.01 ± 0.03	0.14 ± 0.01 ± 0.03	0.13 ± 0.01 ± 0.02	0.24 ± 0.01 ± 0.05	0.21 ± 0.01 ± 0.02
[Zn/H]	0.15 ± ... ± 0.05	0.12 ± ... ± 0.03	0.18 ± ... ± 0.08	0.15 ± ... ± 0.04
[S/H]	0.23 ± 0.09 ± 0.09	0.20 ± ... ± 0.05	0.20 ± ... ± 0.05	...	0.12 ± 0.02 ± 0.03	0.22 ± 0.02 ± 0.05	0.20 ± 0.03 ± 0.05
[Cu/H]	0.02 ± ... ± 0.05	-0.09 ± ... ± 0.05	0.14 ± ... ± 0.05	0.18 ± ... ± 0.05	-0.02 ± ... ± 0.03	0.28 ± ... ± 0.08	0.22 ± ... ± 0.04
[K/H]	0.34 ± ... ± 0.05	0.31 ± ... ± 0.05	...	0.12 ± ... ± 0.05	0.29 ± ... ± 0.03	...	0.18 ± ... ± 0.04
[N/H]	0.06 ± ... ± 0.05	0.08 ± ... ± 0.03

^b σ_μ - the uncertainty in the mean

^c σ_{Total} - quadratic sum of σ_μ and uncertainties due to T_{eff} , $\log g$, and ξ .

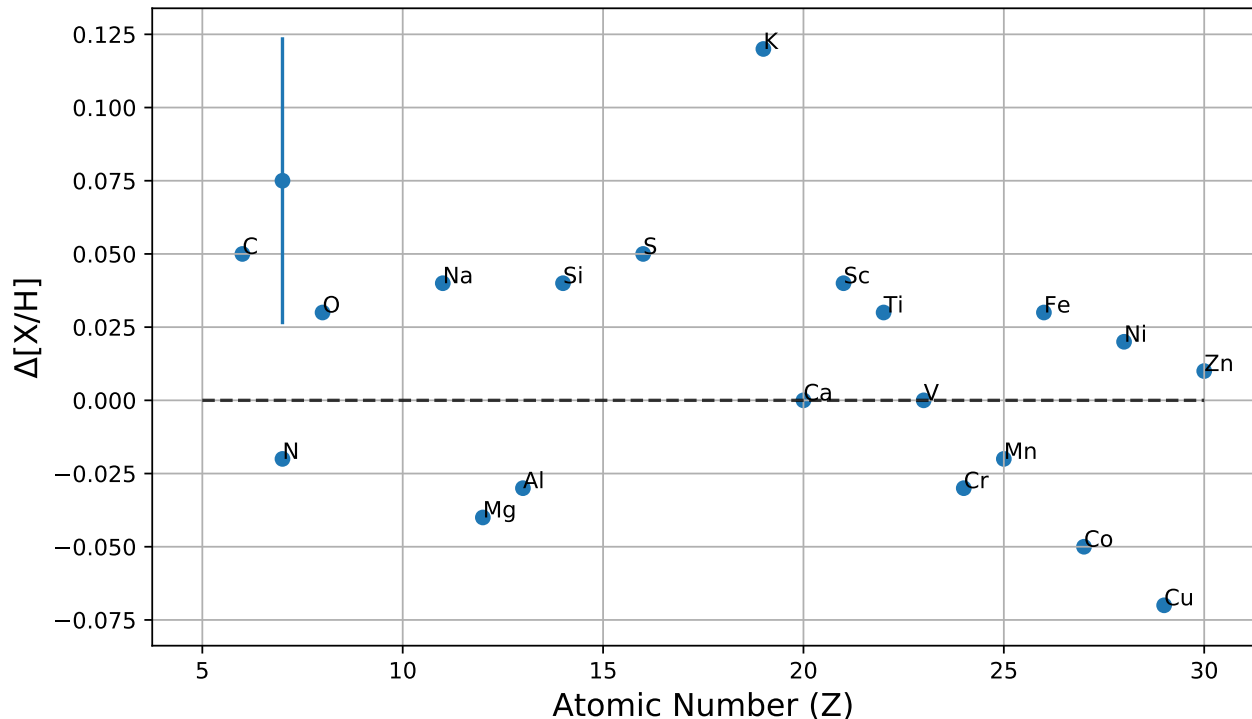


Fig. 8.— Abundance difference between planet host (Pr0201) and cluster mean vs. atomic number for all elements. Dashed line denotes zero difference and the average error is shown in the top left corner, which shows the $\pm 1\sigma$ error with a dot to mark the center.

3.1.2. Non Planet-Hosting Stars

In Figure 9 we show the difference between each star and the cluster mean (the mean not including that specific star). Elements noted below are considered overabundant or deficient if they are more than 1σ (in actual errors, not average errors) different from zero.

Pr0133 is only overabundant in K by 0.08 dex and deficient in C by 0.07 dex, Ti by 0.07 dex, Sc by 0.11 dex, and Cu by 0.20 dex.

Pr0208 has the highest metallicity of our analysed stars, $[\text{Fe}/\text{H}]$ of 0.26 dex, and shows an overabundance in many elements: S by 0.04 dex, Ni by 0.05 dex, Ti by 0.06 dex, Cr by 0.06 dex, Na by 0.07 dex, Mg by 0.07 dex, Al by 0.07 dex, Sc by 0.09 dex, and Co by 0.14 dex. While elements of high condensation temperature tend to be overabundant in Pr0208, the high error bars on the volatile elements make it difficult to say if there is any overall trend with condensation temperature.

Pr0081 shows an overabundance in C by 0.06 dex and Cu by 0.13 dex. Deficient elements include: Si by 0.03 dex, Al by 0.04 dex, Na by 0.08 dex, and K by 0.16 dex.

Pr0051 shows no overabundance but many deficiencies: Cr by 0.04 dex, Si by 0.05 dex, Ni by 0.05 dex, Ti by 0.05 dex, V by 0.08 dex, Fe by 0.06 dex, Mg by 0.07 dex, Co by 0.06 dex, S by 0.09 dex, Mn by 0.09 dex, and Cu by 0.11 dex.

Pr0076 shows deficiencies in C by 0.06 dex and K by 0.08 dex while being overabundant in: Cr by 0.04 dex, Na by 0.05 dex, Al by 0.05 dex, Ni by 0.05 dex, Ca by 0.06 dex, Mn by 0.11 dex, and Cu by 0.17 dex.

3.2. Comparison to Previous Work

An et al. (2007) determined $[\text{Fe}/\text{H}]$ of four G type dwarfs in Praesepe through spectroscopy (equivalent width method) and photometry (photometric metallicity). The mean $[\text{Fe}/\text{H}]$ they determined through spectroscopy ($+0.11 \pm 0.03$) was lower than our determined mean metallicity of 0.21 ± 0.02 . The $[\text{Fe}/\text{H}]$ they determined through photometry ($+0.20 \pm 0.04$) is in much better agreement with our results and most current literature values.

Pace et al. (2008) performed a detailed chemical study of eight elements (Fe, Na, Al, Si, Ca, Ti, Cr, Ni) on 20 solar-type stars in four open clusters, obtaining high resolution ($R=100\text{K}$) and high signal to noise ($S/N = 130$) data for seven stars in Praesepe (with two overlapping stars; Pr0133 and Pr0201). They measure a higher mean Fe abundance of $+0.27 \pm 0.10$, though still within errors of our mean abundance. For Pr0201, all eight elements agree within errors, while Pr0133 shows less agreement. Half of the elements agree with our results (Ca, Ti, Cr, Fe) while the other half (Na, Al, Si, Ni) are higher in abundance than our measurements. Our Al measurement comes from just one absorption line for Pr0133 with the total error being the average of the other elements, this could mean this error is underestimated. It is unclear why there is such a discrepancy in the other elements. All reported mean abundances relative to Fe are within error bars except for O which is much lower than our determined abundance.

Carrera & Pancino (2011) studied abundances of three giants in Praesepe using the equivalent width method and while they measure a lower mean $[\text{Fe}/\text{H}]$ abundance of $+0.16 \pm 0.05$ dex, this mean does fall within errors of our determined mean. Many of the other abundances relative to Fe (Al, Ca, Co, Cr, Mg, Na, Ni, Sc, Si, Ti, and V) disagree with our results having higher abundances except in the case of Ti and Ca. This is likely due to the fact that these stars are of different stellar type than ours and the lower measured metallicity would increase the abundance ratios relative to Fe.

Boesgaard et al. (2013) presented chemical abundances of 16 elements (Li, C, O, Na, Mg, Al, Si, Ca, Sc, Ti, V, Cr, Fe, Ni, Y, and Ba) for 11 solar-type stars in Praesepe (with four overlapping stars; Pr0133, Pr0208, Pr0081, and Pr0076) through equivalent width analysis. They determined a mean cluster metallicity of $+0.12 \pm 0.04$ dex, which is lower than our determined mean by 0.09 dex. Abundance ratios for other elements relative to Fe are within 1σ of our measurements except for Al and Sc. In most cases the abundance ratios are higher in value, likely because of the lower mean $[\text{Fe}/\text{H}]$ abundance. In Pr0133, Pr0208, and Pr0076, our study overlaps with 13 elements (excluding Li, Y, and Ba) while Pr0081 overlaps with 12 elements (excluding Mg as well). For Pr0133, all elements agree within errors except for Sc, which was found to be about solar or higher (0.04 ± 0.08 dex) while we derived a sub-solar value (-0.20 ± 0.08 dex). For Pr0208, errors are not reported in this study, but most elements agree within our own errors. Two elements that do not agree within our errors are Sc and Ti; however, if the errors on these elements are at all similar to the errors for the other stars reported in Boesgaard et al. (2013) then it is very likely they would agree with our abundances. Abundances for Pr0081 are also presented without errors and similarly to Pr0208, all derived abundances (Fe, C, O, Na, Al, Si, Ca, Sc, Ti, V, Cr, and Ni) are within our own errors except for Sc. It is also true that if the errors for this star are similar to the other stars, Sc would also fall within the errors. For Pr0076, all 13 elements fall within reported errors.

Gebran et al. (2019) used an automated spectral analysis code (BACCHUS) to determine abundances

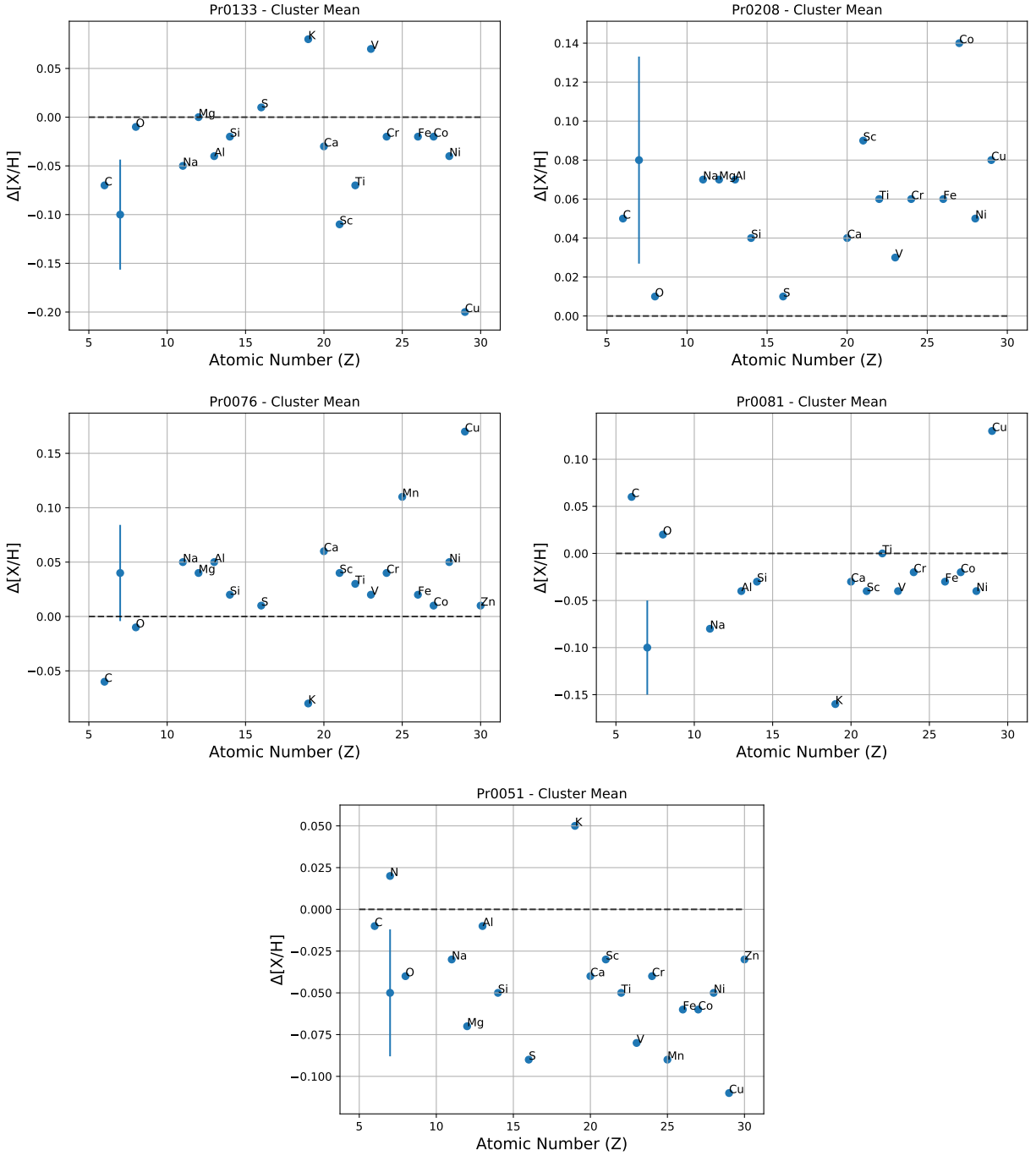


Fig. 9.— Abundance difference between each other star in Praesepe and cluster mean vs. atomic number for all elements. Dashed line denotes zero difference and the average error is shown on the left of each plot, which shows the $\pm 1\sigma$ error with a dot to mark the center.

of 24 elements for five stars in Praesepe (with three overlapping stars; Pr0133, Pr0081, and Pr0076). They report mean abundances for G and K stars separately, $+0.17 \pm 0.04$ and $+0.12 \pm 0.01$ dex respectively. These means are consistent with each other and the literature, the average for G types is consistent with our work. In Pr0133 and Pr0081, our study overlaps with 14 elements (C, O, Na, Mg, Al, Si, Ca, Sc, Ti, V, Cr, Co, Ni, and Cu), all of which agree within errors for Pr0081. For Pr0133, all elements but Na and Cu agree within errors. Our $[\text{Na}/\text{Fe}]$ abundance is about solar or less (-0.07 ± 0.07 dex) while Gebran et al. (2019) determined an even lower abundance of -0.35 ± 0.16 dex. The reverse is true for Cu, our work derived a very low abundance of -0.28 ± 0.09 dex while Gebran et al. (2019) derived a solar or higher value of 0.02 ± 0.03 dex. For Pr0076, our study overlaps with 17 elements (Fe, C, O, Na, Mg, Al, Si, Ca, Sc, Ti, V, Cr, Mn, Co, Ni, Cu, Zn), all of which also fall within reported errors.

D’Orazi et al. (2020) revisited the metallicity of Praesepe taking high-resolution spectroscopic observations of 10 solar-type dwarf stars, including Pr0208. All eight elements (Fe, Na, Mg, Al, Si, Ca, Ti, and Ni) studied are within errors of our derived abundances for Pr0208. They report a mean metallicity of $+0.21 \pm 0.01$ dex and conclude that Praesepe is the most metal-rich, young open cluster in the solar neighborhood, in remarkable agreement with our results that also gives confidence in works that report a higher metallicity. Pr0051 has no literature values to be compared to but the general agreement of our results to the literature gives us confidence in those values as well.

Even with similar analyses the literature suggests a large scatter in metallicity for Praesepe, however, each individual work shows a much lower scatter within their respective sample. The scatter within these works (for $[\text{X}/\text{Fe}]$), including our own, is largely consistent with what we would expect from open clusters (Kovalev et al. 2019; De Silva et al. 2007; Bovy 2016). This implies that the Praesepe cluster is chemically homogeneous and these works may be self-consistent but they may not all be consistent with each other. As our analyses and precision improve, it seems we may converge on a consistent metallicity for Praesepe, perhaps a larger sample analyzed consistently could shed more light on the mean and scatter for the cluster.

3.3. Chemical Homogeneity of Praesepe

In Table 6 we show the $[\text{X}/\text{H}]$ and $[\text{X}/\text{Fe}]$ abundance mean, standard deviation, and error in the mean for our stars in Praesepe. For most of the elements, the $[\text{X}/\text{Fe}]$ standard deviation and the error in the mean are lower than either for $[\text{X}/\text{H}]$. A few exceptions are the elements C, N, O, and Zn which show a lower $[\text{X}/\text{H}]$ standard deviation and error in the mean. K shows the same standard deviation and error in the mean in both $[\text{X}/\text{H}]$ and $[\text{X}/\text{Fe}]$. The average standard deviation is ~ 0.01 dex lower in $[\text{X}/\text{Fe}]$ than $[\text{X}/\text{H}]$, while the average error in the mean is about the same. In $[\text{X}/\text{Fe}]$, the standard deviation of most elements is at or below the average ~ 0.02 - 0.03 dex, well within literature limits on open cluster abundance scatter (De Silva et al. 2007; Bovy 2016; Kovalev et al. 2019). With this, we verify that the stars in our sample are chemically homogeneous; a larger sample would be required to confirm the chemical homogeneity of Praesepe as a whole. C and N are above the average by ~ 0.02 dex. K and Cu are much higher than the average by ~ 0.04 and ~ 0.06 dex respectively. Looking at the error in the mean we see a similar separation where most elements are below the average at ~ 0.01 - 0.02 dex with elements N, K, and Cu being ~ 0.03 dex higher than the average. C and Mn are above the mean by ~ 0.01 dex or less.

For elements with $Z > 19$ (Ca, Sc, Ti, V, Cr, Mn, Co, Ni, Zn), the scatter in both standard deviation and error in the mean is higher for odd-Z elements (Sc, V, Mn) with the exception of Co which is similar to Ca, Ti, and Cr, but higher than Ni and Zn. This is likely due to the fact that some of these odd-Z elements

may have 1-2 synthetically measured absorption lines for each star to account for hfs effects along with lines measured normally where hfs effects are negligible.

4. Discussion

Differential abundances studies often compare the abundances of a planet host with that of a wide stellar companion assumed to have formed of the same cloud of material (Ramírez et al. 2011; Tucci Maia et al. 2014; Mack et al. 2014). The resulting differences are attributed to processes occurring after the stars have formed such as planet formation, system evolution, and stellar evolution. Generally, open clusters are assumed to be chemically homogeneous (De Silva et al. 2006; Boesgaard et al. 2013) (which we verify for our sample in section 3), here we have the rare opportunity to compare our planet host Pr0201 with not just one stellar companion, but five other stars that formed from the same cloud with no known planets.

4.1. Abundance Trends and Condensation Temperature

In the search for planet formation signatures we specifically focus on trends in refractory elements with $T_C > 900\text{K}$ (Meléndez et al. 2009). During early disk evolution, elements with high T_C are expected to condense into solids at shorter distances from the host star, leading to refractory-poor gas and refractory-rich planetesimals. This results in two possible abundance signatures for the host star. The removal of these elements from the protoplanetary disk allows the accretion of the refractory-depleted material onto the host star which imparts a decreasing trend in the refractory elements with T_C . Alternatively, accretion of refractory-rich planetesimals or planets themselves would impart an increasing trend.

In this section we interpret condensation temperature trends in the context of a planet engulfment model, explained in Mack et al. (2014), based on the addition or removal of material with similar composition as the Earth to/from the convection zone of a solar-type star. The composition of the Earth is taken from McDonough (2001) and solar composition is from Asplund et al. (2009). We adjust the size of the convection zone based on the temperature of the star according to Pinsonneault et al. (2001). Solar abundances are modified to match those of the cluster mean (excluding Pr0201) then we can adjust the number of M_\oplus accreted/sequestered in order to produce a desired T_C slope.

Figure 10 shows the T_C trend for refractory elements of the cluster mean. Here, we have excluded the planet host, Pr0201, to show that the mean cluster abundances alone present no trend with condensation temperature. The cluster mean abundances show a slope of $-5.98 \times 10^{-6} \pm 3.25 \times 10^{-5} \text{dex/K}$ consistent with zero slope. When comparing each other star with the cluster mean (excluding that star and the planet host in the mean), no star shows a statistically significant trend in refractory elements with condensation temperature (slopes shown in Fig 11).

We will take a closer look at Pr0201, because it is the only known planet-host in our sample. Figure 12 shows the T_C trend for refractory elements in the planet host Pr0201 relative to the cluster mean. The best fit line to these elements gives a negative slope of $-8.64 \times 10^{-5} \pm 6.59 \times 10^{-5} \text{dex/K}$. While not a statistically significant detection (1.3σ), if taken at face value, this trend could be explained by the sequestering of $\sim 1.62 M_\oplus$ of material from the convection zone of Pr0201.

Our T_C slope results are relative to solar abundances ($[X/H]$), meaning a slope consistent with zero tells us the distribution of abundances with respect to T_C is similar to that of the sun. Results for the cluster

Table 6. Abundance Scatter

[X/Y]	Mean	Std	Error in Mean
[C/H]	0.082	0.045	0.02
[C/Fe]	−0.125	0.048	0.021
[N/H]	0.07	0.01	0.01
[N/Fe]	−0.125	0.045	0.045
[O/H]	0.082	0.02	0.009
[O/Fe]	−0.125	0.029	0.013
[Na/H]	0.158	0.047	0.021
[Na/Fe]	−0.048	0.024	0.011
[Mg/H]	0.176	0.041	0.021
[Mg/Fe]	−0.036	0.029	0.015
[Al/H]	0.145	0.037	0.016
[Al/Fe]	−0.062	0.03	0.014
[Si/H]	0.165	0.03	0.014
[Si/Fe]	−0.042	0.009	0.004
[S/H]	0.19	0.037	0.018
[S/Fe]	−0.022	0.026	0.013
[K/H]	0.248	0.084	0.042
[K/Fe]	0.052	0.084	0.042
[Ca/H]	0.193	0.031	0.014
[Ca/Fe]	−0.013	0.02	0.009
[Sc/H]	0.083	0.056	0.025
[Sc/Fe]	−0.123	0.036	0.016
[Ti/H]	0.189	0.04	0.018
[Ti/Fe]	−0.017	0.021	0.01
[V/H]	0.223	0.039	0.018
[V/Fe]	0.017	0.034	0.015
[Cr/H]	0.223	0.03	0.014
[Cr/Fe]	0.017	0.023	0.01
[Mn/H]	0.193	0.058	0.041
[Mn/Fe]	−0.01	0.043	0.031
[Fe/H]	0.207	0.033	0.015
[Co/H]	0.153	0.056	0.025
[Co/Fe]	−0.053	0.38	0.017
[Ni/H]	0.17	0.034	0.015
[Ni/Fe]	−0.037	0.014	0.006
[Cu/H]	0.075	0.112	0.05
[Cu/Fe]	−0.132	0.104	0.047
[Zn/H]	0.14	0.014	0.01
[Zn/Fe]	−0.063	0.017	0.012
[X/H] _{avg}		0.043	0.021
[X/Fe] _{avg}		0.035	0.018

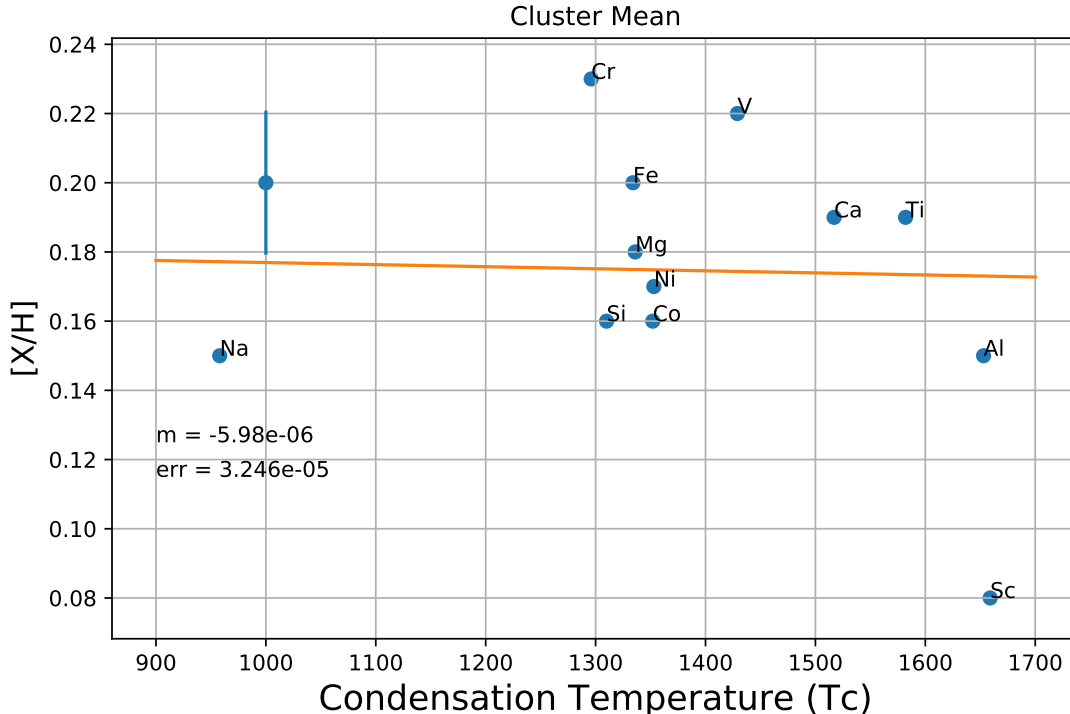


Fig. 10.— Cluster mean vs. condensation temperature (T_C) for refractory elements excluding the planet host Pr0201. The average error is shown on the top left, which shows the $\pm 1\sigma$ error with a dot to mark the center.

mean T_C slope are consistent with zero slope meaning the cluster abundance distribution may be similar to the sun. This could indicate that planet-formation for sun-like stars in the cluster is common or that the cluster initially formed from a cloud with this distribution already in place. The possible discovery of more planets within the cluster could give more weight to the prominent planet-forming case. All six of our analyzed stars, including the known planet-host, show a slope consistent with zero when compared to the cluster mean. If planet formation is in fact prevalent, the lack of detected planets in our sample could be due to the difficulty of finding smaller planets or these systems may have lost their planets entirely.

4.2. Limits on Chemical Signatures of Planet Ingestion in Pr0201

The Pr0201 system is host to a short period (4.4264 ± 0.0070 days) gas giant (Pr0201b) with a minimum mass of $0.54 \pm 0.039 M_J$ in a circular orbit (Quinn et al. 2012). With such a close-in giant planet and a T_C slope consistent with zero, we investigate the possibility that Pr0201 could have accreted or sequestered refractory-rich material during the planet formation process. Using our planet engulfment model mentioned above, we can place limits on the amount of this material. To do this, we assume Pr0201 formed with the same composition as the cluster mean, starting off with zero slope in the refractory elements. We then add material with the same composition as the Earth until we produce a significant T_C slope (3σ using the measured error in the T_C slope for Pr0201) in the refractory elements (shown in the top panel of Figure 13). In order to produce a statistically significant T_C slope, Pr0201 would have needed to accrete $4.42 M_\oplus$ of

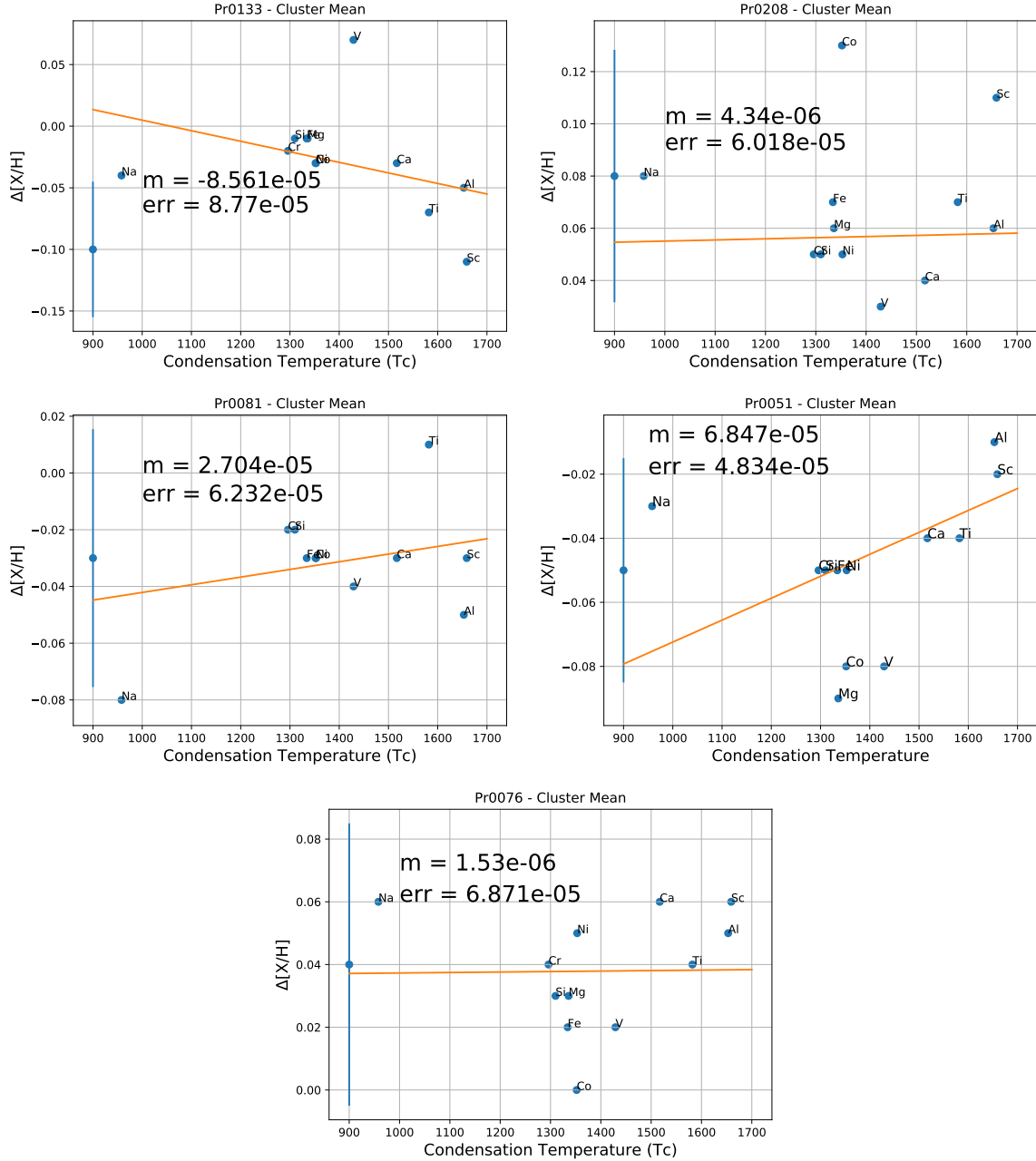


Fig. 11.— T_c trend between each other star and cluster mean for refractory elements. The average error is shown on the left of each plot, which shows the $\pm 1\sigma$ error with a dot to mark the center.

material. In the bottom panel of Figure 13, we show how this would affect the individual refractory elements of the cluster mean, depicted by the orange points and lines, which can be compared to the abundances of Pr0201 in purple. The solid lines show the mean abundance while the dashed lines show \pm the error in the mean. This accretion scenario would produce abundances that are noticeably enhanced compared Pr0201

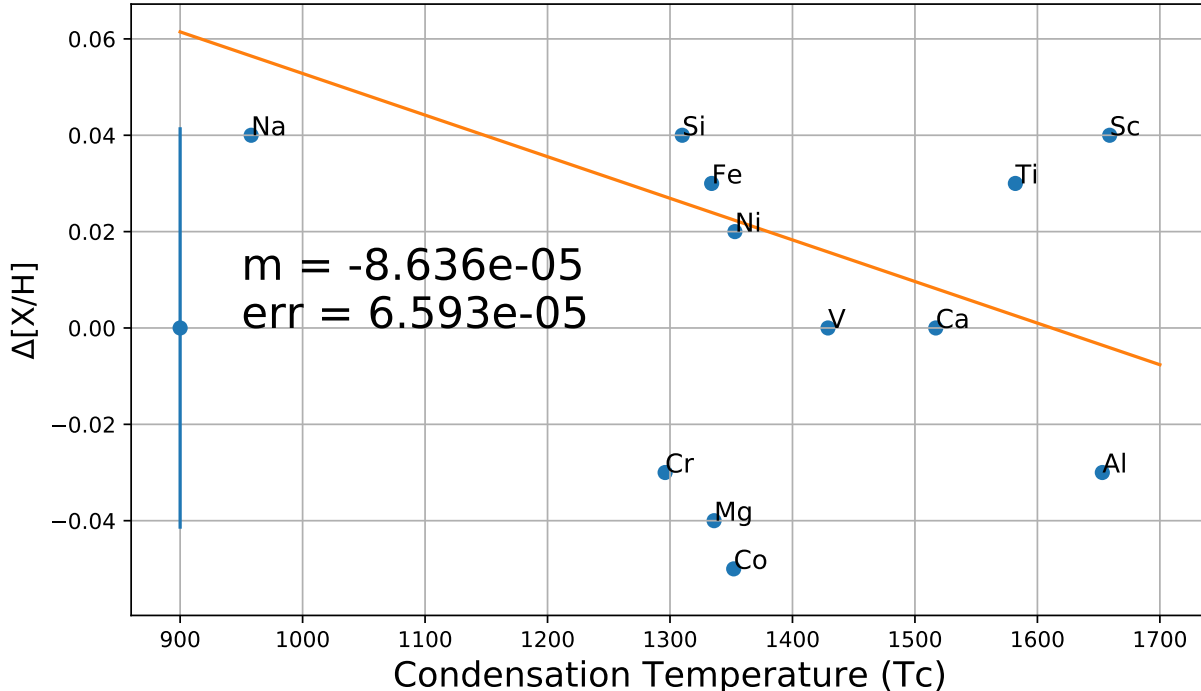


Fig. 12.— T_C trend of the difference between planet host, Pr0201, and cluster mean for refractory elements. The average error is shown on the left side of the plot, which shows the $\pm 1\sigma$ error with a dot to mark the center.

and can be ruled out at the $\sim 16.5\sigma$ level. Excluding Ti, V, and Fe, it is also the case that $1.25 M_{\oplus}$ of material can be ruled out at the 5σ level, indicated by the green lines. In general, Pr0201 does not seem significantly enhanced in refractory elements when compared to the cluster mean. This analysis focuses on accretion but can also be applied to material sequestered.

5. Conclusion

In this work we have used new Keck/HIRES observations combined with KOA spectra of six G or F type stars, one of which hosts a $0.54 M_J$ giant planet, in the nearby Praesepe Cluster to derive detailed solar-relative elemental abundances with a precision of ~ 0.05 dex. For each star we determined T_{eff} , $\log g$, $[\text{Fe}/\text{H}]$, ξ (microturbulence parameter), and abundances of up to 20 elements (Table 5; Figure 7). We verify that our results are in good agreement with the current literature and determine a mean cluster metallicity of $+0.21 \pm 0.02$ dex.

We made use of a new custom-built python code for EW measurements called XSpect-EW. The code automatically normalizes each order, wavelength shifts the orders to the rest frame, and fits a Gaussian profile to each line of interest while allowing the user to edit and rerun any of these processes with specified parameters when necessary. This makes measuring hundreds of lines much faster as many lines can be measured automatically with little user contribution and helps to remove some user error when manually performing these tasks.

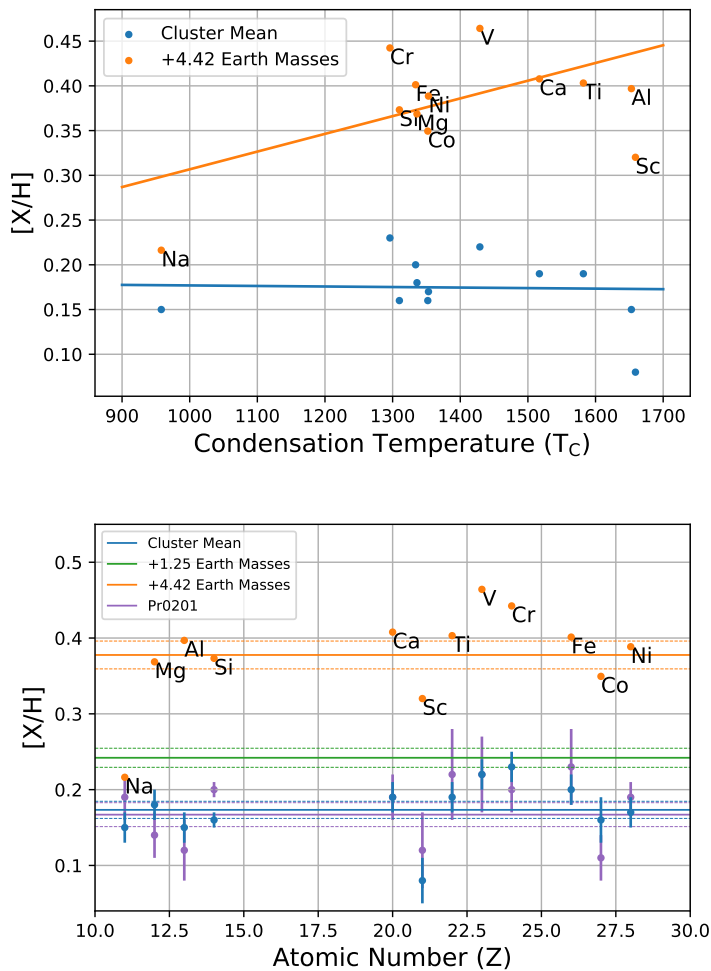


Fig. 13.— Top panel: The refractory cluster mean abundances (excluding Pr0201) are shown in blue vs T_C along with simulated abundances (orange) of the addition of 4.42 M_\oplus to the cluster mean, which would produce a statistically significant slope at the 3 sigma level. Bottom panel: Cluster mean abundances are shown in blue vs atomic number along with the average (solid line) and \pm the error in the mean (dashed lines). Green and orange lines denote the addition of different amounts of M_\oplus . Purple points show the abundances for Pr0201, the planet host.

We find no T_C trend in the mean cluster abundances (Figure 10). Comparing each star’s individual elemental abundances with the cluster mean abundances we see a negative T_C trend in the planet host, Pr0201, of $-8.64 \times 10^{-5} \pm 6.59 \times 10^{-5}$ dex/K. According to our planet engulfment model, the slope in Pr0201 corresponds to the sequestering of 1.62 M_\oplus of terrestrial material from the convection zone of the star which could be an indication of terrestrial planet formation, although no terrestrial planets have been detected for this star. We conclude that Pr0201 likely did not accrete a significant amount of Earth-like material.

As mentioned in the introduction, a natural dependence on cluster size and structure is prominent in

determining the strength of the chaotic effects of the cluster environment on planet formation and survival. Praesepe, being an open cluster, contains less mass than a globular cluster, only about $\sim 600 \pm 19 M_{\odot}$ (Adams et al. 2002). Less mass would dictate fewer O/B stars could initially form, lowering the effect of photoevaporation on disks, stellar winds and supernovae on gas expulsion, and impart a lower average velocity on the cluster members lowering the frequency of stellar encounters. Even in high density environments, short period planets can survive throughout the lifetime of the cluster (Cai et al. 2019). Cluster environmental effects on planet survivability are still not completely understood; however, the current picture painted by recent studies is one of planet formation being common and most of them surviving the evolution of the cluster (albeit in smaller sized systems or as free-floating planets, most of which are expected to escape the cluster; e.g., van Elteren et al. 2019). Combined with the high metallicity of Praesepe, we have reason to believe that planets could be abundant in the cluster. Already, studies have found 13 planets in Praesepe and about 30 total planets in open clusters (Cai et al. 2019). Pfalzner & Vincke (2020) reported that our solar system likely formed in a high-mass extended or intermediate-mass compact association like NGC 6611 or Praesepe, due to roughly 10% of solar-type stars experiencing flyby’s after which a solar system analog would remain. As RV surveys become more precise, we expect many more planets will be discovered in nearby open clusters.

The authors acknowledge support by NSF AAG AST-1009810 and NSF PAARE AST-0849736. This research has made use of the Keck Observatory Archive (KOA), which is operated by the W. M. Keck Observatory and the NASA Exoplanet Science Institute (NExScI), under contract with the National Aeronautics and Space Administration. This work makes use of the Radial Velocity Simulator accessed through the Astronomy Education at the University of Nebraska-Lincoln Web Site (<http://astro.unl.edu>). We thank the LSSTC Data Science Fellowship Program which has benefited this work. George Vejar also thanks Karl Jaehnig for his help and support which benefited this work.

REFERENCES

- Adams, J. D., Stauffer, J. R., Skrutskie, M. F., et al. 2002, *AJ*, 124, 1570
- An, D., Terndrup, D. M., Pinsonneault, M. H., et al. 2007, *ApJ*, 655, 233
- Anderson, K. R., Adams, F. C., & Calvet, N. 2013, *ApJ*, 774, 9
- Anthony-Twarog, B. J., Lee-Brown, D. B., Deliyannis, C. P., et al. 2018, *AJ*, 155, 138. doi:10.3847/1538-3881/aaad66
- Asplund, M., Grevesse, N., Sauval, A. J., & Scott, P. 2009, *ARA&A*, 47, 481
- Biazzo, K., Gratton, R., Desidera, S., et al. 2015, *A&A*, 583, A135. doi:10.1051/0004-6361/201526375
- Boesgaard, A. M., Roper, B. W., & Lum, M. G. 2013, *ApJ*, 775, 58
- Boesgaard, A. M., Lum, M. G., Deliyannis, C. P., et al. 2016, *ApJ*, 830, 49. doi:10.3847/0004-637X/830/1/49
- Boesgaard, A. M., Lum, M. G., & Deliyannis, C. P. 2020, *ApJ*, 888, 28. doi:10.3847/1538-4357/ab4fdb
- Bovy, J. 2016, *ApJ*, 817, 49. doi:10.3847/0004-637X/817/1/49
- Cai, M. X., Kouwenhoven, M. B. N., Portegies Zwart, S. F., et al. 2017, *MNRAS*, 470, 4337
- Cai, M. X., Portegies Zwart, S., Kouwenhoven, M. B. N., et al. 2019, *MNRAS*, 489, 4311
- Cantat-Gaudin, T., Jordi, C., Vallenari, A., et al. 2018, *A&A*, 618, A93. doi:10.1051/0004-6361/201833476
- Carrera, R. & Pancino, E. 2011, *A&A*, 535, A30
- D’Orazi, V., Oliva, E., Bragaglia, A., et al. 2020, *A&A*, 633, A38
- Davis, B. D., Bond, H. E., Ciardullo, R., et al. 2019, *ApJ*, 884, 115. doi:10.3847/1538-4357/ab44d4
- Delorme, P., Cameron, A. C., Hebb, L., et al. 2011, 16th Cambridge Workshop on Cool Stars, Stellar Systems, and the Sun, 448, 841
- De Silva, G. M., Sneden, C., Paulson, D. B., et al. 2006, *AJ*, 131, 455. doi:10.1086/497968
- De Silva, G. M., Freeman, K. C., Asplund, M., et al. 2007, *AJ*, 133, 1161. doi:10.1086/511182
- François, P., Pasquini, L., Biazzo, K., et al. 2013, *A&A*, 552, A136. doi:10.1051/0004-6361/201220958
- Fujii, M. S. & Hori, Y. 2019, *A&A*, 624, A110
- Gaia Collaboration, Brown, A. G. A., Vallenari, A., et al. 2018, *A&A*, 616, A1. doi:10.1051/0004-6361/201833051
- Gebran, M., Agüeros, M. A., Hawkins, K., et al. 2019, *ApJ*, 871, 142
- Geller, A. M., Latham, D. W., & Mathieu, R. D. 2015, *AJ*, 150, 97. doi:10.1088/0004-6256/150/3/97
- González-Díaz, D., Moni Bidin, C., Silva-Villa, E., et al. 2019, *A&A*, 626, A10. doi:10.1051/0004-6361/201935243
- Haworth, T. J., Clarke, C. J., Rahman, W., et al. 2018, *MNRAS*, 481, 452

- Henden, A. A., Welch, D. L., Terrell, D., et al. 2009, American Astronomical Society Meeting Abstracts #214
- Johansen, A., Davies, M. B., Church, R. P., et al. 2012, *ApJ*, 758, 39
- Johnson, J. A., Ivans, I. I., & Stetson, P. B. 2006, *ApJ*, 640, 801
- Johnson, J. A., Aller, K. M., Howard, A. W., et al. 2010, *PASP*, 122, 905. doi:10.1086/655775
- Kovalev, M., Bergemann, M., Ting, Y.-S., et al. 2019, *A&A*, 628, A54. doi:10.1051/0004-6361/201935861
- Kupka, F., Piskunov, N., Ryabchikova, T. A., et al. 1999, *A&AS*, 138, 119. doi:10.1051/aas:1999267
- Kurucz, R. 1993, ATLAS9 Stellar Atmosphere Programs and 2 km/s grid. Kurucz CD-ROM No. 13. Cambridge, 13
- Lin, D. N. C., Bodenheimer, P., & Richardson, D. C. 1996, *Nature*, 380, 606
- Liu, F., Asplund, M., Yong, D., et al. 2016, *MNRAS*, 463, 696. doi:10.1093/mnras/stw2045
- Lum, M. G. & Boesgaard, A. M. 2019, *ApJ*, 878, 99. doi:10.3847/1538-4357/ab1c4d
- Mack, C. E., III, Schuler, S. C., Stassun, K. G., & Norris, J. 2014, *ApJ*, 787, 98
- Mack, C. E., Stassun, K. G., Schuler, S. C., et al. 2016, *ApJ*, 818, 54. doi:10.3847/0004-637X/818/1/54
- Martin, C., Barlow, T., Barnhart, W., et al. 2003, *Proc. SPIE*, 4854, 336. doi:10.1117/12.460034
- Maurya, J. & Joshi, Y. C. 2020, *MNRAS*, 494, 4713. doi:10.1093/mnras/staa893
- Mayor, M., & Queloz, D. 1995, *Nature*, 378, 355
- McDonough, W. 2001, in *The Composition of the Earth, in Earthquake Thermodynamics and Phase Transitions in the Earth's Interior* (International Geophysics Series, Vol. 76), ed. R. Teisseyre & E. Majewski (San Diego, CA: Academic Press)
- MacLean, B. T., De Silva, G. M., & Lattanzio, J. 2015, *MNRAS*, 446, 3556. doi:10.1093/mnras/stu2348
- Meibom, S., Torres, G., Fressin, F., et al. 2013, *Nature*, 499, 55
- Meléndez, J., Asplund, M., Gustafsson, B., & Yong, D. 2009, *ApJ*, 704, L66
- Monteiro, H. & Dias, W. S. 2019, *MNRAS*, 487, 2385. doi:10.1093/mnras/stz1455
- Naoz, S. 2016, *ARA&A*, 54, 441
- Pace, G., Pasquini, L., & François, P. 2008, *A&A*, 489, 403
- Pacucci, F., Ferrara, A., & D’Onghia, E. 2013, *ApJ*, 778, L42
- Piskunov, N. E., Kupka, F., Ryabchikova, T. A., et al. 1995, *A&AS*, 112, 525
- Pfalzner, S., Bhandare, A., & Vincke, K. 2018, *A&A*, 610, A33
- Pfalzner, S. & Vincke, K. 2020, *ApJ*, 897, 60
- Pinsonneault, M. H., DePoy, D. L., & Coffee, M. 2001, *ApJ*, 556, L59

- Prochaska, J. X., & McWilliam, A. 2000, *ApJ*, 537, L57
- Quinn, S. N., White, R. J., Latham, D. W., et al. 2012, *ApJ*, 756, LL33
- Ramírez, I., Meléndez, J., & Asplund, M. 2009, *A&A*, 508, L17
- Ramírez, I., Meléndez, J., Cornejo, D., Roederer, I. U., & Fish, J. R. 2011, *ApJ*, 740, 76
- Ramírez, I., Khanal, S., Aleo, P., et al. 2015, *ApJ*, 808, 13. doi:10.1088/0004-637X/808/1/13
- Ramírez, I., Khanal, S., Lichon, S. J., et al. 2019, *MNRAS*, 490, 2448. doi:10.1093/mnras/stz2709
- Reddy, A. B. S., Giridhar, S., & Lambert, D. L. 2015, *MNRAS*, 450, 4301. doi:10.1093/mnras/stv908
- Saffe, C., Flores, M., & Buccino, A. 2015, *A&A*, 582, A17. doi:10.1051/0004-6361/201526644
- Saffe, C., Jofré, E., Martioli, E., et al. 2017, *A&A*, 604, L4. doi:10.1051/0004-6361/201731430
- Sandquist, E. L., Jessen-Hansen, J., Shetrone, M. D., et al. 2016, *ApJ*, 831, 11. doi:10.3847/0004-637X/831/1/11
- Schuler, S. C., King, J. R., & The, L.-S. 2009, *ApJ*, 701, 837. doi:10.1088/0004-637X/701/1/837
- Schuler, S. C., Cunha, K., Smith, V. V., et al. 2011, *ApJ*, 737, L32
- Schuler, S. C., Vaz, Z. A., Katime Santrich, O. J., et al. 2015, *ApJ*, 815, 5
- Skrutskie, M. F., Cutri, R. M., Stiening, R., et al. 2006, *AJ*, 131, 1163. doi:10.1086/498708
- Snedden, C. A. 1973, Ph.D. Thesis
- Snedden, C., Uomoto, A., Cottrell, P., et al. 2012, *Astrophysics Source Code Library*. ascl:1202.010
- Stassun, K. G. & Torres, G. 2016, *AJ*, 152, 180. doi:10.3847/0004-6256/152/6/180
- Teske, J. K., Ghezzi, L., Cunha, K., et al. 2015, *ApJ*, 801, L10. doi:10.1088/2041-8205/801/1/L10
- Tucci Maia, M., Meléndez, J., & Ramírez, I. 2014, *ApJ*, 790, L25. doi:10.1088/2041-8205/790/2/L25
- van Elteren, A., Portegies Zwart, S., Pelupessy, I., et al. 2019, *A&A*, 624, A120. doi:10.1051/0004-6361/201834641
- Vogt, S. S., Allen, S. L., Bigelow, B. C., et al. 1994, *Proc. SPIE*, 2198, 362
- Winter, A. J., Clarke, C. J., Rosotti, G., et al. 2018, *MNRAS*, 478, 2700
- Wright, E. L., Eisenhardt, P. R. M., Mainzer, A. K., et al. 2010, *AJ*, 140, 1868. doi:10.1088/0004-6256/140/6/1868
- Zheng, X., Kouwenhoven, M. B. N., & Wang, L. 2015, *MNRAS*, 453, 2759